Politecnico di Torino

Corso di Laurea Magistrale in Ingegneria Aerospaziale

Modeling of an innovative actuation system for high lift devices and its control logic

Advisors:
Matteo Davide Lorenzo Dalla Vedova
Matteo Bertone
Alessandro Aimasso
Paolo Maggiore

Candidate:
Alessio Rostagno
319930

A.Y. 2024/2025

1 Abstract

The aim of this thesis is to analyse the applicability of an electric actuation system to control the secondary moving surfaces of a business jet, specifically the Lockheed Jetstar. In the study, different mechanical irreversibility devices are implemented, including the No-Back Brake and the Wing-Tip Brake, in order to guarantee the safety of the system. The model of the actuation system, developed in the MATLAB/Simulink environment, is based on a non-distributed configuration of the high-lift devicet acuation system. Control logics were also modelled to manage and limit any asymmetries between the two sides of the wing during the operation of the secondary moving surfaces, a critical requirement for the design of actuation systems.

Contents

List of Figures

2 Introduction

The aim of this thesis is to prove that an electro-mechanical actuation of the high lift devices is possible on a business jet such as the Lockheed JetStar.

2.1 Flight commands principles

Flight controls are an essential part of the aircraft's onboard systems for manoeuvrability and controllability. There are essentially two types of flight control systems: primary and secondary. Each category has its own specific operating characteristics, a brief description is now provided.

Primary controls:

1. are continuous proportional controls;
2. modify the aircraft's trajectory by generating torques around the body axes;
3. must provide the pilot with appropriate feedback on the action of the control and must be instinctive in order to facilitate the setting of the manoeuvre;
4. must be extremely reliable, otherwise the aircraft will become uncontrollable and must provide an adequate frequency response.

Secondary controls:

1. are on-off controls capable of assuming a limited number of discrete positions and are occasionally activated during take-off and landing manoeuvres;
2. modify the aerodynamic coefficients of the wing;
3. must be able to maintain the position selected by the pilot continuously;
4. in the event of a possible failure, the controllability of the aircraft must be guaranteed.

In the classic aircraft configuration, each type of flight control corresponds to a series of related surfaces. The control surfaces operated by the primary flight controls are:

- Ailerons;
- Elevators;
- Rudder.

The control surfaces operated by the secondary flight controls are:

- High-lift devices (flaps, slats);
- Spoilers and air-brakes;
- Stabilisers.

The latter division of control surfaces is not as distinct as in the past. New innovative aerodynamic configurations, especially in military aircraft, use control surfaces that do not correspond to the standard classification above.

This thesis refers to secondary flight controls for moving high-lift surfaces (flaps) in standard aircraft configuration, using an electromechanical actuation system.

2.2 Flap-slat actuation system possible failures

The actuation system for high-lift surfaces may be subject to certain specific types of failures, such as:

- **Flap-Slat Asymmetry**: asymmetrical extension or retraction of the moving surfaces, a phenomenon essentially related to the disconnection of a torsion bar in the kinematic chain. Even the seizure of a single actuator can cause the movement of a single surface to degenerate (each surface is moved by at least two actuators), in which case we refer to skewed extension. The effect on the aircraft is manifested by asymmetry in the lift between the wings, with possible loss of aircraft controllability and structural damage. The possible solution is to implement monitoring and control systems capable of activating systems that can lock the moving surfaces in a relative position that ensures an acceptable margin of controllability.
- **Flap Runaway**: a condition of flap extension or retraction not controlled by the pilot, which results in a loss of lift and, in certain conditions, aircraft stall. The solution to the problem prevents selections in the pilot control lever controlled by the control system, which in turn prevents the retraction of the servomechanism during take-off and landing depending on the speed of the aircraft. Our requirement is for the engagement of irreversibility devices for premature retraction within a tolerance of 3 degrees.
- **Flap Overspeed**: each angle of extension of the moving surfaces is associated with a maximum IAS (Indicated Air Speed), which must not be exceeded due to the dangerous increase in torque acting on the moving surfaces and the entire wing structure.
- **Power Control Unit Failures**: Each movement system provides for dual mechanical power generation supplied independently by different lines. In the event of failure of one of the PCU units, the remaining unit is capable of moving both mechanical lines of the movable surfaces connected to it. If both power units or the connecting gear box are unable to operate, the safety system intervenes by blocking the compromised hydraulic lines, canceling the delivery pressure and thus activating the hydraulic brakes of the transmission lines and drive shafts. Failures of the PDUs or individual actuators are generally more frequent, but usually only result in the movement system becoming inoperative and do not statistically represent a critical issue for flight safety. On the other hand, the loss of integrity of the mechanical movement line due, for example, to the breakage of a torsion bar generates, if not controlled by appropriate emergency systems, large extraction asymmetries, which represent a highly critical phenomenon for the safety of the aircraft as they considerably limit controllability.

This document analyses the condition that poses the greatest danger to flight safety: Flap Extension Asymmetry, caused mainly by the failure of an element of the kinematic handling chain. In the event of a breakage of one of the torsion bars that transmit mechanical power to the reversible actuators, the array of moving surfaces downstream of the breakage is subject to high aerodynamic load. In the absence of drive torque, the moving surface is subject exclusively to high hinge torque, which the forces of friction and inertia are unable to compensate for. Therefore, the surface recedes from the position it assumed until the moment of failure, with considerable actuation speed. The surfaces still mechanically connected to the gearbox in the case of engines coupled in pairs are moved by twice the torque at design speed, a phenomenon that accentuates the onset of symmetry between the moving surfaces. Overall, the phenomenon degenerates into a broad symmetry that requires failure detection and intervention systems capable of promptly locking the moving surfaces in order to reduce the possibility of developing high extraction asymmetry.

2.3 Flight accidents due to flap control failures

Among the countless accidents attributable to malfunctions of the high-lift device system, we mention below the most significant ones from the statistics for the years 2008, 2009 and 2010. All of the following accidents are attributable to asymmetry in the deployment of high-lift devices:

- **03/10/2010**: British Airways Boeing 747–400 registered G-CIUIK on the Sydney-Bangkok route, due to asymmetry in flap deployment, was forced to make a fast emergency landing after take-off, damaging the landing gear.
- **15/06/2010**: Akerfly Boeing 767-300 at Toronto airport made an emergency return due to asymmetry in flap deployment during take-off. Damage to the landing gear and minor injuries to three passengers were reported.
- **04/09/2009**: KDAVIA Boeing 737-300 at Kaliningrad airport detected asymmetry in flap extension control of 7 degrees, right flap extended to 15 degrees while left flap extended to 22 degrees. Following the emergency landing, the landing gear was destroyed and the aircraft was severely damaged. Fortunately, no injuries were reported among the passengers or crew.
- **27/01/2009**: An Empire Airline ATR42-320 at Lubbock Airport, Texas, during landing, recorded asymmetrical extension of the flaps with relative loss of control of the aircraft and crash landing. Serious damage to the aircraft, which was beyond repair, and serious injuries to the two crew members.
- **01/10/2008**: Boeing 747 registered G-B1GA at Johannesburg airport during take-off, uncommanded retraction of the leading edge surfaces was recorded for approximately 23 seconds, with a risk of aircraft stall. Thanks to the pilot's previous experience in aerobatics, the crew managed to land without injury to passengers or further damage to the aircraft.
- **19/03/2008**: PREMIER I 390 UTRAL at Udaipur Airport in India, asymmetric flap opening was detected, resulting in an emergency landing with an excessively high approach speed. Serious damage to the landing gear and left wing was detected, with injuries to the co-pilot.

Despite the innovations introduced in the control and monitoring of servo controls for movement, there is a clear need to develop and improve further strategies to reduce a significant statistic relating to the asymmetry of high-lift surfaces, with the aim of improving flight safety. Controlling extraction asymmetry is essential because, in addition to limiting the controllability of the aircraft in critical phases such as take-off and landing, under certain operating conditions it can lead to catastrophic events that cannot be compensated for by modern computerised aircraft control systems and crew expertise. To emphasise the importance of the design of high lift surface control systems, reference is made to document A06Q0188 -D1-C1 of 21 February 2007 issued by the Canadian Transportation Safety Board, which examines the statistics on high-lift system failures for the entire CRJ fleet consisting of Bombardier CJ200 and CJ100 aircraft. These statistics report as many as 48 incidents in 2005 and 2006, on the basis of which the Canadian Transportation Safety Board urges a complete review and improvement of the flap and slat movement system.

2.4 Lockheed JetStar and its configuration

The Lockheed JetStar is a pioneering business jet that first took flight in 1957 and became one of the earliest dedicated executive jet aircraft. Developed by Lockheed Aircraft Corporation, it was designed to meet the U.S. Air Force's requirement for a small jet transport and quickly found favor in the civilian market due to its performance, range, and spacious cabin. Powered by four turbojet or turbofan engines mounted at the rear

Figure 1: Lockheed Jetstar

fuselage, the JetStar is instantly recognizable by its distinctive configuration featuring a high T-tail and wingtip fuel tanks, which contribute to its long-range capabilities. The original models were equipped with Pratt & Whitney JT12 engines, while later versions featured more fuel-efficient Garrett TFE731 turbofan engines, improving both range and operating costs.

The JetStar can typically accommodate 8 to 10 passengers in a comfortable, pressurized cabin designed for executive travel. Its large size for the time, combined with long-range performance and a relatively high cruising speed, made it a popular choice among corporate and government operators.

Though production ended in the 1970s, and the aircraft is no longer in widespread use, the Lockheed JetStar remains a significant milestone in business aviation history—marking the transition to the jet age for corporate and VIP air travel.

Max Speed (Mach)	0.82
Cruising Speed (km/h)	805
Service Ceiling (m)	13100
Max Range (km)	5185
Takeoff Distance (m)	1830
Landing Distance (m)	1310

The Lockheed JetStar employed a relatively conventional but effective high-lift system to improve low-speed performance, particularly during takeoff and landing phases. Its configuration was characteristic of early-generation business jets and optimized for stability, reliability, and manufacturability.

The airplane used double-slotted Fowler flaps, mounted on the trailing edge of the wing. These flaps extend rearward and downward, increasing both wing area and camber, which significantly enhances lift at lower speeds. The double-slotted design creates a gap between the flap segments and the wing, allowing high-energy air from below the wing

to re-energize the boundary layer over the flap, delaying flow separation and allowing for higher lift coefficients.

The flaps were actuated using a system of gearboxes, torque shafts, and actuators, with built-in asymmetry protection. A no-back brake system was integrated into the drive train to prevent flap retraction under aerodynamic loads if power was lost or if load reversal occurred. Flap positions were selectable by the pilot, in several detents such as 0°, 10°, 20°, 30° and full (around 40°).

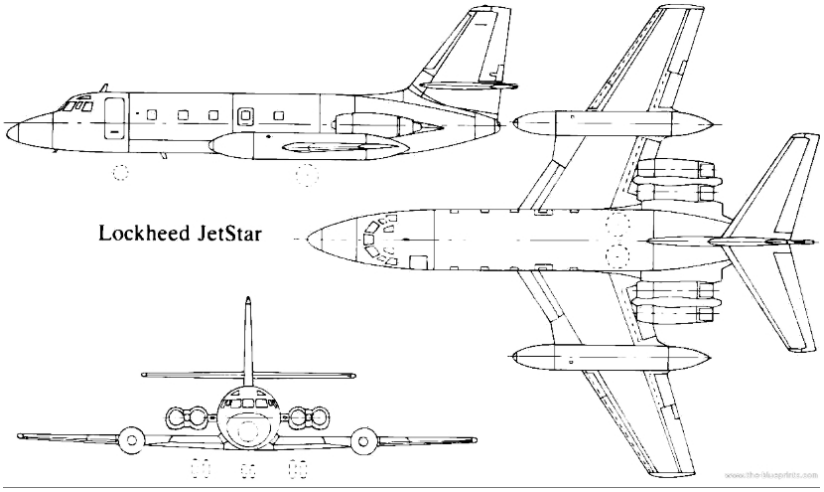

Figure 2: Lockheed Jetstar drawing

2.5 EMA vs. EHA

Electromechanical actuators (EMAs) and Electrohydraulic actuators (EHAs) are two types of actuators used to convert electrical signals into mechanical motion. While both serve similar functional purposes, they differ significantly in design, operating principles, performance characteristics, and ideal use cases.

EMAs use electric motors (usually stepper or servo motors) combined with mechanical components like gears, screws, or belts to produce linear or rotary motion; while EHAs use motors to drive hydraulic pumps, which then generate hydraulic pressure to move a piston or other hydraulic mechanism. In EMAs the power transmission is purely through mechanical means,in EHAs, power is transmitted via hydraulic fluid, which provides the force necessary to move the actuator. The latter is typically better suited for high-force applications due to the inherent strength of hydraulic systems and generally provide faster and stronger responses for large loads. EMAs are generally limited in force output, especially in compact systems, but offer good performance for moderate-load applications. But EMAs offer excellent precision and repeatability, as motor position and movement can be finely controlled through electrical signals. EMAs may have slower response times under heavy loads but excel in applications requiring high accuracy and moderate force. EHAs can also offer good control, especially with modern electronics, but are generally less precise than EMAs due to fluid compressibility and other dynamic factors. For a maintenance and complexity perspective the EMAs are typically simpler and more compact, with fewer components and lower maintenance requirements, since they don't rely on fluids or pumps; instead the EHAs are more complex, requiring hydraulic lines, seals, reservoirs, and pumps, which may need more frequent maintenance and present a higher risk of leaks. Talking of sustainability, EMAs are cleaner and more environmentally friendly, as they don't involve fluids that could leak or contaminate the environment, while EHAs carry the risk of hydraulic fluid leakage, which can be a concern in sensitive environments like aerospace or food processing.

Considering the weight of the actuation system, it can be seen that for small aircraft applications, where aerodynamic loads are moderate, Electromechanical Actuators (EMAs) would be the best choice because, compared to EHAs, the total weight of the system would be lower, as the fluid, piping and hydraulic pumps are not involved.

2.6 Electrical motor

For this case study, it was decided to use the BLDC model 4.0-154 motor produced by the Chinese company Volcano Electric. The BLDC motor was chosen because it requires less maintenance and has a longer operating life.

This motor has the following operational data:

Supply voltage (V)	48
Max current (A)	92
Max torque (Nm)	14.81
Speed (rpm)	2580

2.7 PID controller

The proportional-integral-derivative control unit, identified by the acronym PID, represents the logical architecture used to improve the dynamic characteristics of a negative feedback system, in order to satisfy the prescribed operating conditions by improving the degree of stability and response speed of the system for different forms of control signals. A position feedback loop simulation system compares the position of the controlled element with the commanded position at each instant of time, defining the position error magnitude.

The components of the PID controller, located upstream of the system to be controlled, use the time trend of the error E(t) to define the control action. The control actions are schematized in three blocks placed in parallel and use three numerical constants KP, KI, and KD, corresponding to the proportional, integral, and derivative actions operating on the signal. The control actions are schematized in three blocks placed in parallel and use three numerical constants KP, KI, and KD, corresponding to the actions: proportional, integral, and derivative operating on the input signal of the position error.

The three actions of a PID are calculated separately and added together in a command signal addressed to the electric motor controller.

In detail, the actions of the controller are as follows:

- Proportional action: the proportional action is obtained by multiplying the position error by the controller parameter, which in the proposed model is indicated by GAP according to the formula:

$$U_P = KPe(t) \tag{2.1}$$

  The proportional contribution performs its function in short and medium-term phenomena, reducing both the rise time (i.e., increasing the system's response readiness) and the steady-state error, without however eliminating it due to positioning errors caused by the non-linearity of the system.

- Integrative action: The integral action is proportional to the integral of the error signal over time, multiplied by the constant KI divided by an integral time constant I. In practice, the integrative controller acts on the sum of the position error over time, performing its useful function in the long term, eliminating the steady-state error as indicated in the formula:

$$U_I = KI \int e(t)dt \tag{2.2}$$

- Derivative Action: Derivative action compensates for variations in the error signal over time, therefore it does not act with a constant error other than zero, as it does not intervene to satisfy the stationarity requirements of the command. Although the derivative compensator always provides a stabilizing contribution to the system by increasing its damping contribution, it is sensitive to electromagnetic disturbances and fast dynamics in which the error variation is very high. The output provided by the derivative is described by the following formula:

$$U_D = KI \frac{d}{dt} e(t) \tag{2.3}$$

$$U_{PID} = U_P + U_I + U_D \tag{2.4}$$

The choice of high PID controller parameters allows for an increase in the responsiveness of the system but at the risk of increasing the instability provided by the proportional and integrative contributions. In fact, although it is possible to develop mixed controllers that only involve the introduction of a proportional controller or a proportional-derivative controller, it is not possible to implement a proportional-integral controller exclusively in the absence of a derivative contribution, precisely because of the increased instability of the controlled dynamic system.

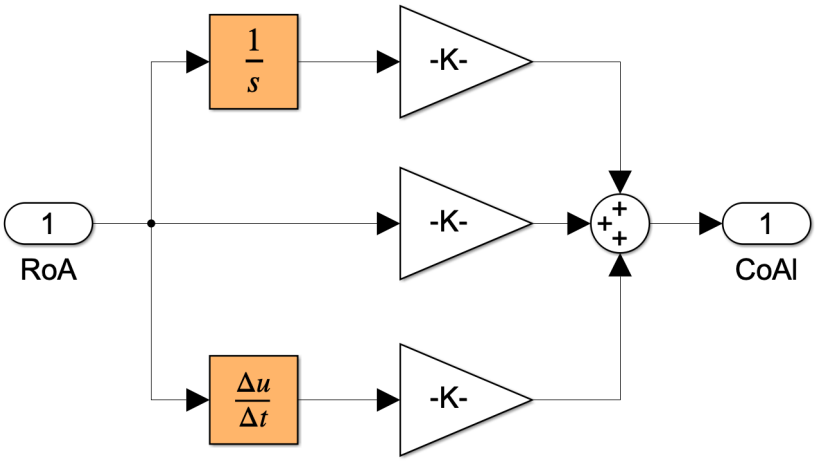

Figure 3: PID controller

3 Friction models and irreversibilities

3.1 Friction models

Friction phenomena between surfaces in relative motion are present in all couplings between physical parts constituting the high-lift surface movement system that is the subject of our analysis.

When creating a simulation model with adequate accuracy, it is not possible to overlook the analysis of friction phenomena, as they have a significant impact on the behaviour of the system, limiting the performance of the position control system. The identification and appropriate modelling of these dissipative phenomena make it possible to improve the precision of the system control, which is capable of processing responses with sufficient accuracy in relation to the actual performance of the physical system. Friction phenomena are a function of the normal load exchanged between the surfaces and the relative sliding speed. Furthermore, the relationships between dry friction forces and the aforementioned speeds are extremely non-linear. Therefore, excessive linearisation would result in a loss of accuracy in the simulation model. For this reason, the study of compensation algorithms to improve performance cannot ignore an in-depth study of the physical phenomenon. The development of models capable of describing the behaviour of the phenomenon under examination must consider not only the relative sliding speed, but also the load exchanged between the parts in contact and the lubrication regime acting between the surfaces. Depending on the sliding speed, the phenomenon can be divided into static friction, in which there is no relative movement between the surfaces, and dynamic friction, in which the surfaces are in relative motion. The friction force exchanged between the surfaces in the two relative speed regimes is described by the following mathematical relationships:

$$StaticFriction : F_s = f_s N \tag{3.1}$$

$$DynamicFriction : F_d = f_d N \tag{3.2}$$

Where:

- f_s = Static friction coefficient;
- f_d = Dynamic friction coefficient;

As regards the dependence of the friction force on the load, as the sliding speed varies, it assumes the minimum value corresponding to the condition of zero load exchanged between the surfaces in contact. In this condition, the friction value is not zero due to various factors such as the necessary construction constraints, in order to reduce or contain mechanical displacement, and the use of seals.

3.1.1 Characteristics of a Friction Model

The development of a comprehensive model of the phenomenon of friction must be able to mathematically describe the behaviour of the mechanical element, discriminating between the following kinematic conditions:

- Static condition: the mechanical element, initially at rest, remains in relative motion as a function of the resultant of the loads applied to it;
- Start condition: the mechanical element, initially at rest, starts to move relative to the surfaces, passing from static friction force to dynamic friction force;
- Motion condition: the mechanical element, initially in motion, remains in this state of motion in relation to the resultant of the loads associated with it;
- Stopping condition: the mechanical element initially in motion stops, passing into a condition of zero relative motion.
- Sign condition: in the case of dynamic friction, the system must discriminate the sign of the friction force as a function of the sliding speed.

A friction model capable of satisfying the above conditions allows for the calculation of sufficiently accurate dynamic simulations capable of reproducing the critical operating conditions of the system under analysis. It is preferable to develop Performance Models for friction, capable of providing a global representation of the phenomenon, rather than defining tribological models capable of capturing local effects and dynamics to the detriment of the global behaviour of the system under examination.

3.1.2 Coulomb friction model

The Coulomb model models the phenomenon of dry friction by presenting an F_s value indicating the value of Static Friction, which is significantly higher than the dynamic friction value of the system. The model in question is able to discriminate the direction of application of the friction force, depending on the direction of the sliding velocity, and to discriminate the conditions of adhesion from those of relative motion between the surfaces in contact. The main flaw of the Coulomb model is the presence of a discontinuity in the friction force at the origin, which causes numerical instability problems in algorithms that use the actuation speed as a numerical derivation of the position signal sampled by the dedicated transducer. This model does not consider the lubrication present between the surfaces.

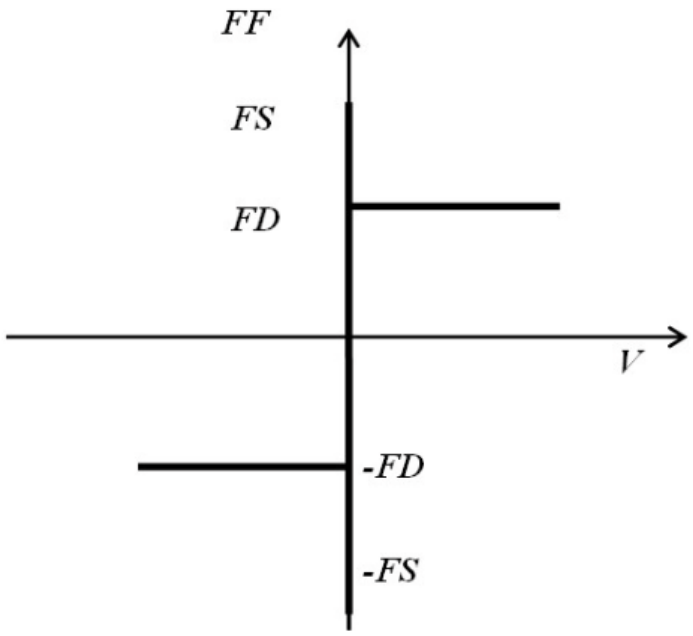

Figure 4: Coulomb friction model

It is possible to implement the branches of the descriptive diagram by implementing linear sections typical of a Viscous Friction Model, which provides a linear relationship between the resistive force and the relative sliding speed.

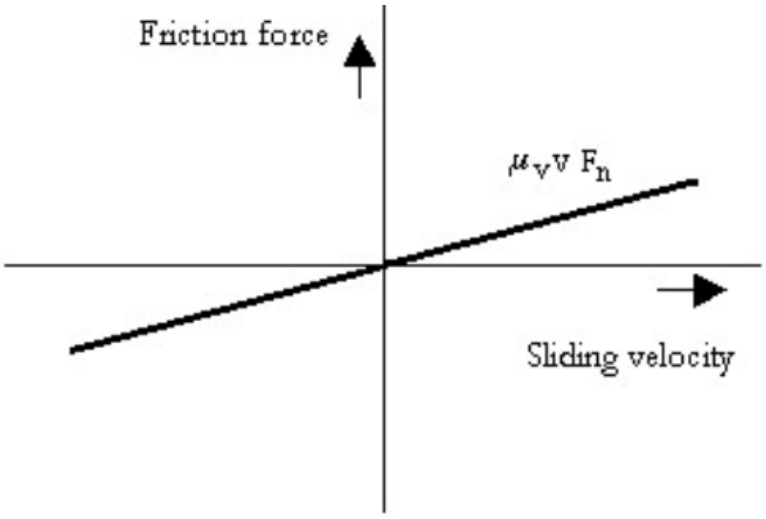

Figure 5: Pure viscous friction model

If we consider a viscous model without implementing the Coulomb model, we obtain a model that predicts zero friction force at zero sliding speed. The results provided are not very accurate in representing the physical reality in which it is possible for there to be no relative motion between surfaces in the presence of friction forces of considerable intensity that cannot be neglected.

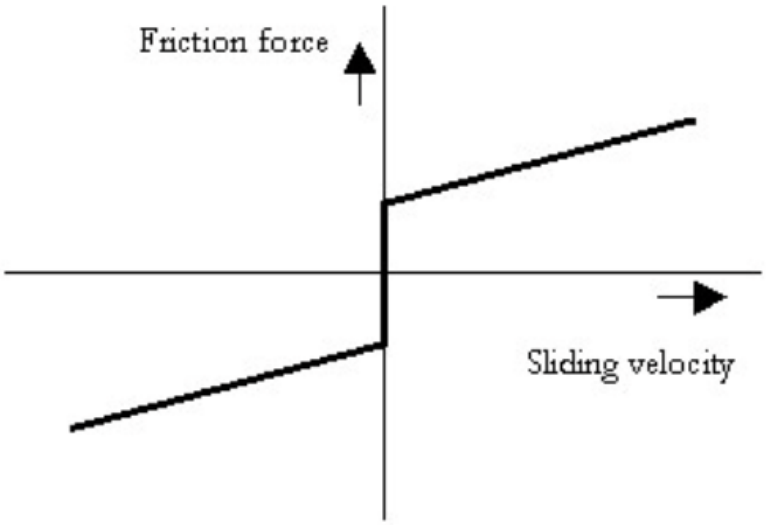

Figure 6: Coulomb friction model with viscosity

3.1.3 Karnopp friction model

The presence of numerical instability, identified as zero crossing problems, as they are associated with discontinuity at the origin, has led to the development of models capable of avoiding the numerical problem. Karnopp's model overcomes the computational problems associated with Coulomb's model by introducing a dead band at the origin centered on the zero velocity value of semi-amplitude ϵ on the velocity axis. Within this band, the velocity is set to zero and the friction force is equal to the minimum between the static friction force F_s value and the maximum value calculated between the resultant of the external forces applied h and the value of $-F_s$ as reported in the following mathematical model:

$$f = \begin{cases} MIN(MAX(-FSJ, h), FSJ) & se \quad |v| \leq \varepsilon \\ v = 0 & se \quad |v| \leq \varepsilon \\ sgn(v) \cdot FDJ & se \quad |v| > \varepsilon \end{cases}$$

Figure 7: Karnopp friction model equations

However, this solution introduces a degree of arbitrariness in defining the width of the dead band, introducing simplifying assumptions that provide a more robust model but with degraded performance in representing low-speed conditions. The guideline to follow in order to define a correct dead band width is to define the bandwidth in the order of magnitude greater than twice the time integration step used. This avoids the risk of having values in an integration step that are equal in modulus but opposite in direction with zero average velocity.

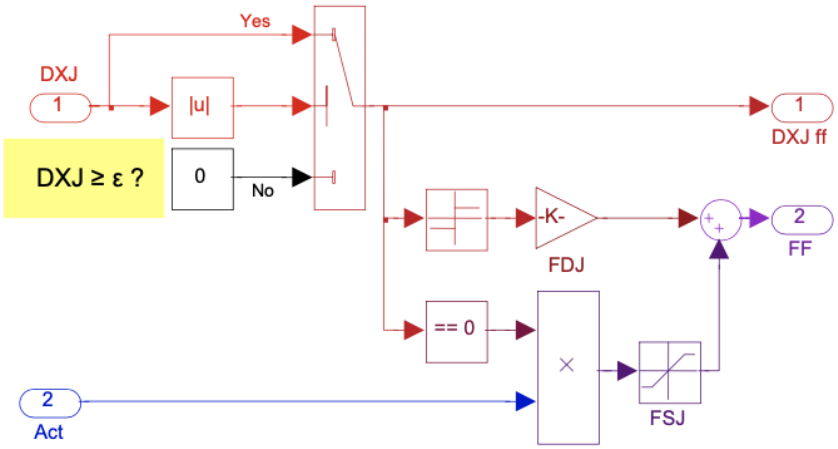

Figure 8: Karnopp friction model on Simulink

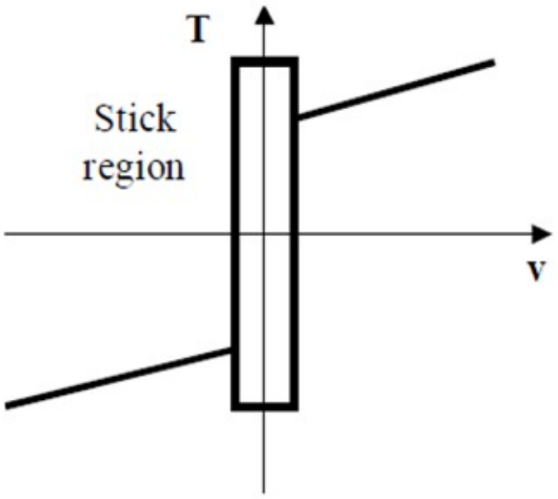

Figure 9: Karnopp friction model

3.1.4 Hyper-viscous friction model

Derived from the Coulomb model, it eliminates the discontinuity at the origin by approximating its trend using a hyper-viscous linear behaviour. In practice, the jump at the origin is replaced by a straight line that emulates the viscous trend seen previously but with an extremely high dimensional viscosity coefficient compatible with the stability of the calculation process. The region of linear behaviour between the friction force and the velocity extends for a half-amplitude ϵ on the horizontal axis. Although it eliminates the problems related to numerical instability due to the presence of jump discontinuities, this model has a serious shortcoming. In fact, the presence of the linear section of the friction force-velocity characteristic implies performance in static conditions that absolutely does not correspond to the Colombian model, which predicts the presence of non-zero static friction forces at zero velocity. In the hyper-viscous model and in all models with linear sections passing through the origin, zero velocity necessarily corresponds to zero friction force, thus rendering the system incapable of balancing any external load applied in static conditions.

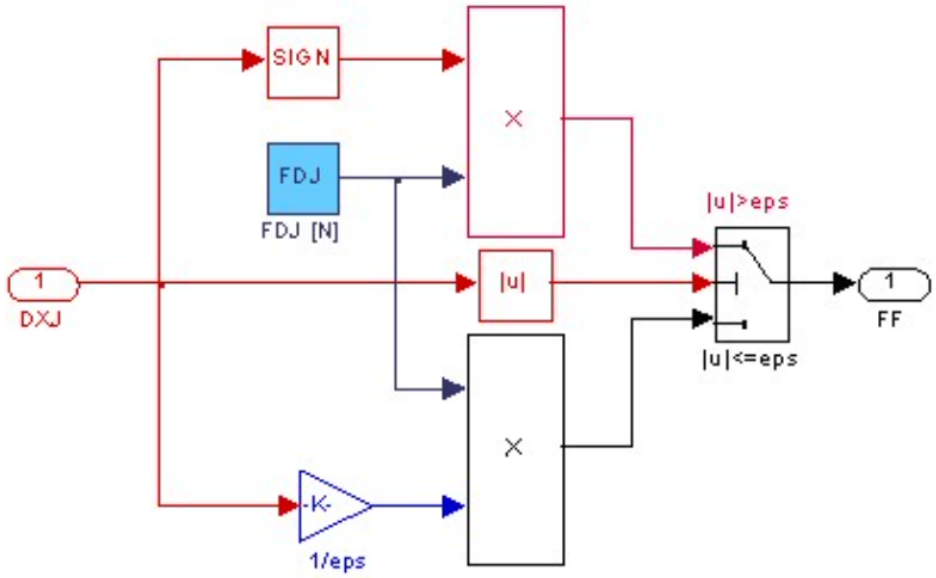

Figure 10: Hyper-viscous friction model on Simulink

Consequently, the application of loads in static conditions, for the simulation of viscous models, implies the creation of accelerations that induce the movement of surfaces in contact, which absolutely does not correspond to the real behaviour of the system, which predicts the presence of static friction forces of non-negligible intensity. This shortcoming inevitably defines this model's inability to correctly distinguish between adhesion and dynamic conditions, to evaluate the possible arrest of the mechanical element in motion, and to maintain static conditions in the presence of a non-zero external load. The development of models similar to the saturated hyper-viscous model has allowed the hybridisation of the linear trend passing through the origin of models that originally assumed the presence of discontinuities at the origin, such as the hyper-viscous version of the Stribeck Model, described in the following section.

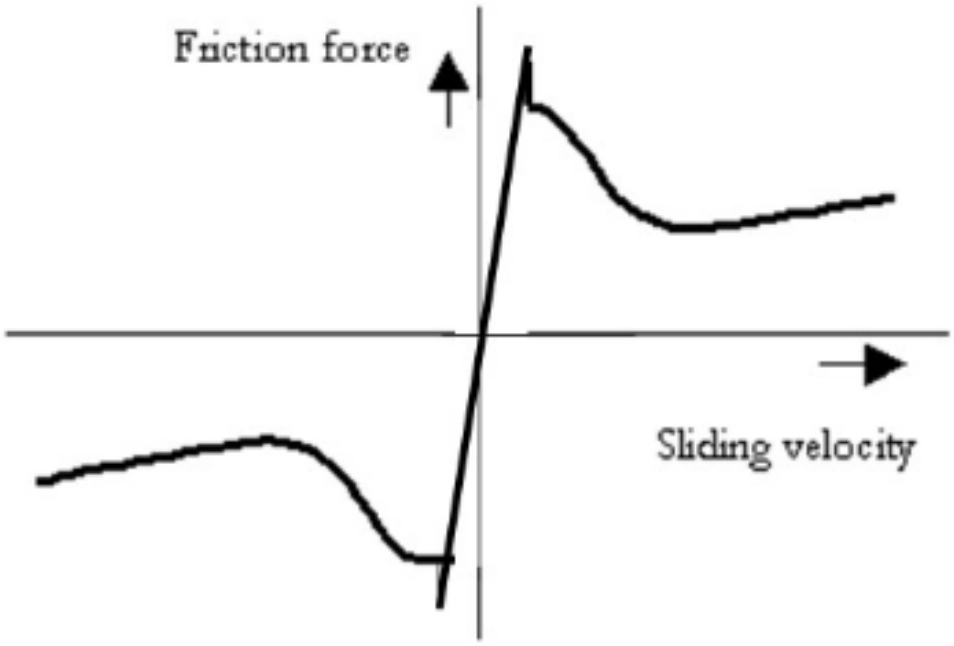

Figure 11: Hyper-viscous friction model

3.1.5 Stribeck friction model

The Stribeck model accurately highlights the behaviour of friction in the presence of partial lubrication between surfaces in relative motion. At low sliding speeds, in the presence of lubricant, four friction regimes are defined corresponding to the four lubrication regimes that make up the Stribeck curve. In particular, four main lubrication regime regions can be distinguished:

1. Static friction
2. Lubrication boundary
3. Partial lubrication
4. Full lubrication

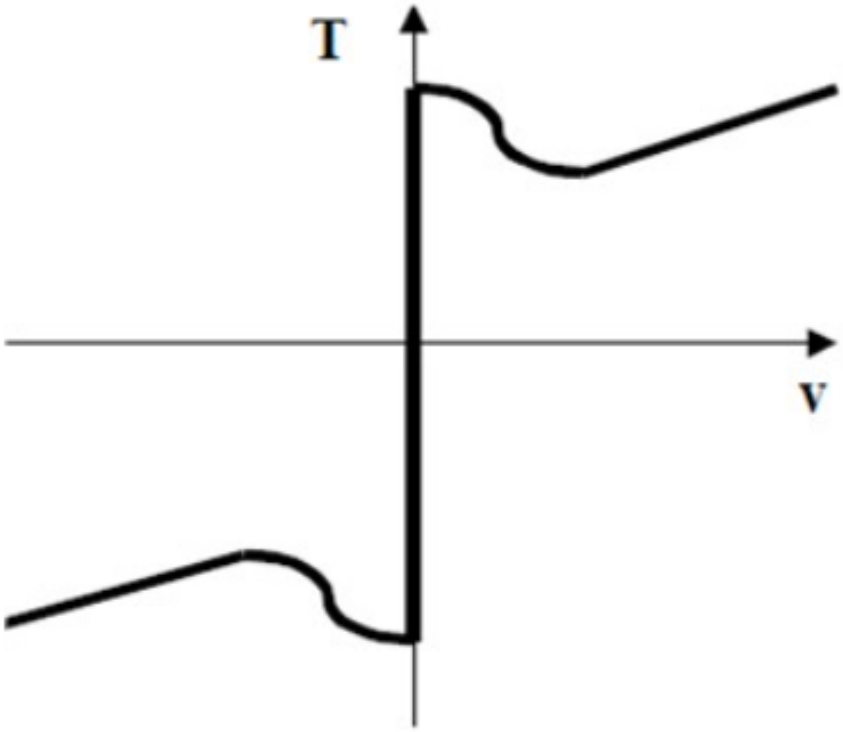

Figure 12: Stribeck friction model

Static friction In the Stribeck model at zero speed, the junctions between the roughnesses present between the contact surfaces can be modelled as springs that hold the surfaces together, and when a load is applied, they deform elastically, causing a pre-slip displacement. This phenomenon occurs until the external load applied exceeds an elastic resistance limit between the roughnesses, triggering motion between the surfaces. The spring stiffness constant that simulates the static interaction between the roughness of the moving surfaces is a function of the geometry of the roughness, the mechanical characteristics of the materials in contact, and the force of contact between the surfaces.

Lubrication boundary This second regime is characterised by an extremely low sliding speed, with no continuous lubrication layer between the two surfaces in direct contact. It is precisely the presence of direct contact between the surface materials that causes the development of a higher friction force than in regimes where there is more consistent lubrication.

Partial Lubrication The movement between the surfaces reaches a characteristic speed at which the lubricating fluid tends to form a layer that is still discontinuous but responsible for a decrease in the friction force, which always opposes the relative movement. The thickness of the lubricating layer is directly proportional to the relative speed and viscosity of the fluid (a function of temperature). This zone is characterised by a negative slope on the Stribeck curve diagram, at which stick-slip phenomena can occur.

Full Lubrication Once the reference speed for entering the full lubrication zone, corresponding to the minimum point of the Stribeck curve, has been exceeded, the two bodies are completely separated from direct contact by the presence of a continuous layer of lubricating fluid. In this region, the characteristic friction force-speed relationship has the linear characteristics typical of viscous dynamic friction.

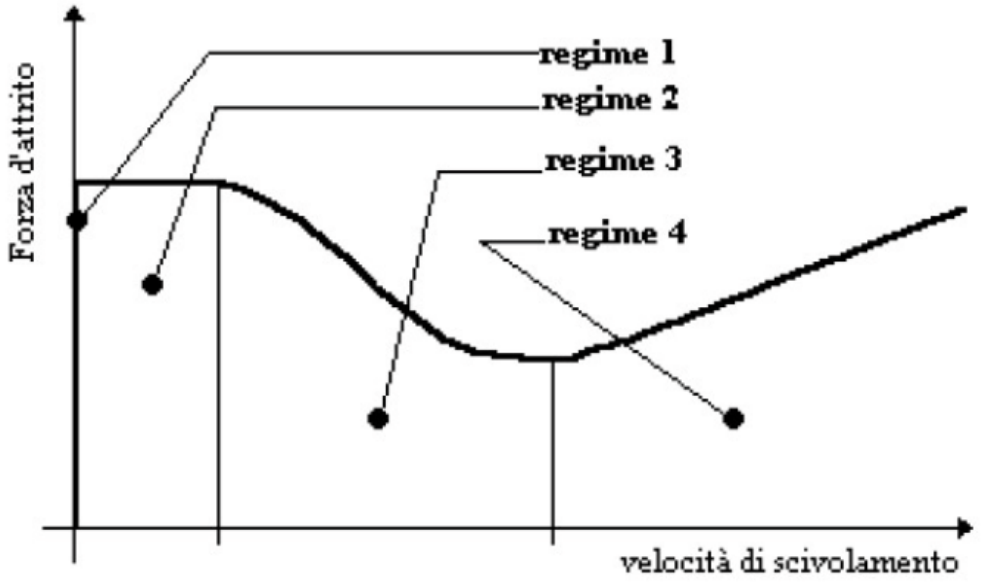

Figure 13: Stribeck main lubrification regime regions

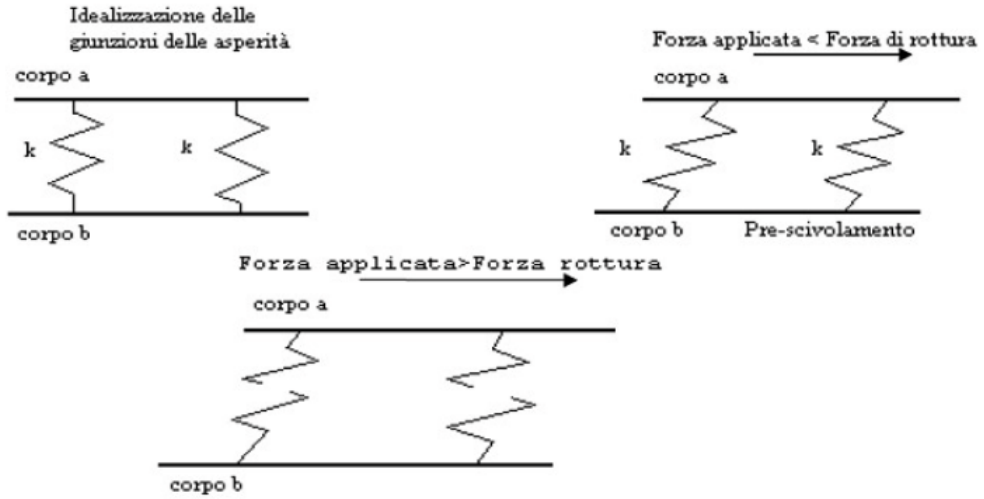

Figure 14: Interactions between two bodies and its correlation with friction

3.1.6 Quinn friction model

The Quinn model aims to evolve the saturated hyperviscous model by eliminating the shortcoming of all linear models passing through the origin, which predict zero friction forces in static conditions. The equations of the Quinn mathematical model are shown below:

$$f = \begin{cases} F \cdot \bar{v} / \varepsilon & se \quad |\bar{v}| \leq \varepsilon \\ \text{sgn}(\bar{v}) \cdot F & se \quad |\bar{v}| > \varepsilon \end{cases}$$

Figure 15: Quinn friction model equations [1]

$$\bar{v} = \begin{cases} v + \varepsilon \cdot h / F & se \quad |h| \leq F \\ v + \text{sgn}(h) \cdot \varepsilon & se \quad |h| > F \end{cases}$$

Figure 16: Quinn friction model equations [2]

The friction force calculated according to the Quinn model is a function of the Coulomb friction force in dynamic conditions F, the relative sliding speed v, the limit speed ε (at which the friction force assumes the saturation value), and the sum of the active forces acting on the system h. The model assumes static conditions, calculating a non-zero value for the friction force only when the absolute value of the forces acting exceeds the friction limit F. For zero values of h, i.e. active forces acting on the system, the Quinn model degenerates into the saturated hyperviscous model, of which it is a special case. Although this model overcomes the shortcomings typical of all models that have a linear section passing through the origin, predicting a non-zero value of the friction force for static conditions, it does not simulate real behaviour at low speeds with sufficient accuracy. Furthermore, the arbitrariness with which the user must set the value of ϵ saturation speed significantly affects the responses of the model under analysis, providing unreliable responses.

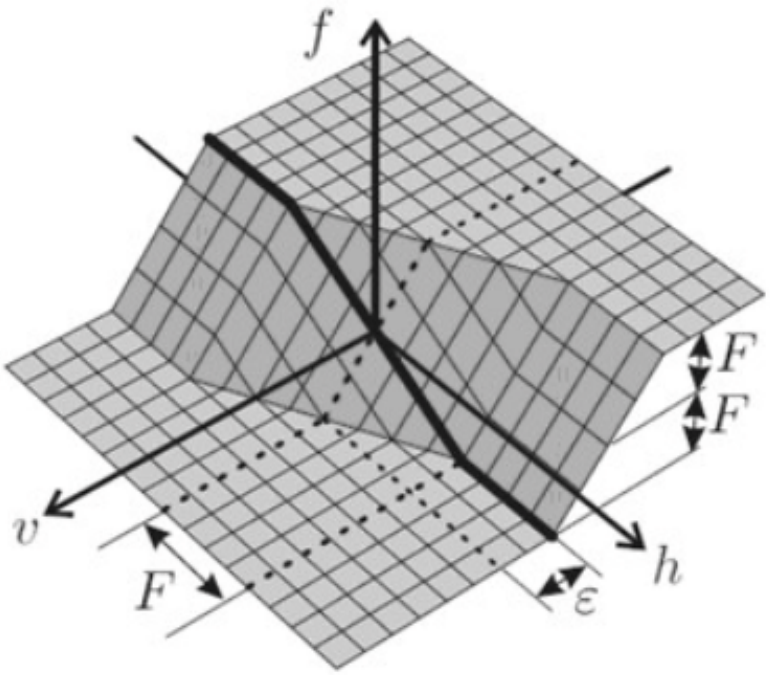

Figure 17: Quinn friction model

The above-mentioned numerical modelling techniques most commonly used in applications and publications found in the literature are based on linearised models that are nevertheless affected by the shortcomings described in detail. The introduction of simplifying assumptions aimed at overcoming the computational problems arising from the presence of discontinuities at the origin in the friction force-velocity characteristic, or from the linear approximation at the origin typical of viscous models, always results in simulation responses that poorly match the actual behaviour of the system, or a certain degree of arbitrariness on the part of the user in defining some sensitive parameters of the model, with the risk of defining a completely unreliable model. In this document, we have chosen to use the Borello Model as a model of friction phenomena, which in the proposed version satisfies both the acceptability criteria for a friction model and avoids the problems arising from previously proposed friction models.

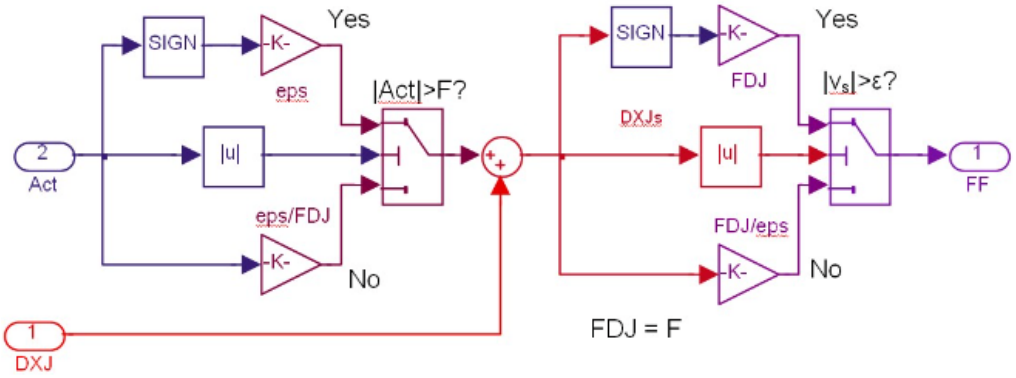

Figure 18: Quinn friction model on Simulink

3.1.7 Borello friction model

In the Borello model, the friction force FF is represented as a function of the active force F_{att} and the sliding speed V. The other quantities that appear in the mathematical

model are: the static friction force F_s, the dynamic friction force F_d, and the resultant of the active forces acting on the system F_{att}.
Analysing the Simulink representation of the model, we can see that a logic block has been inserted that is capable of detecting when a threshold equal to zero speed is crossed. This signal is sent to the first integrator, which outputs the speed value, resetting it for an integration step. In fact, the peculiarity of this model, in order to avoid numerical oscillation phenomena typical of systems represented by discontinuities at the origin, is to stop the mechanical system for one integration step in the presence of a reversal of the speed sign. In the event that the stop imposed for an integration step is not correct, because the active forces acting on the system are greater than those of friction, the next integration step would generate a dynamic starting condition capable of correctly representing the start. In the block model, as long as the decision input of the diverter represents the dynamic friction condition, the system assigns as variable FF the dynamic friction force F_d evaluated in relation to the speed sign calculated by the second-order system. When passing through zero, the gate identifies the crossing of the threshold by sending the zeroing input to the integrator reset, which provides me with the speed for an integration step.
If the stop condition persists, the decision diver assigns the minimum value to the FF variable, derived from the comparison of the resultant of the active forces F_{att} and the first detachment static force F_s.

$$FF = \begin{cases} F_{att} & se \quad v = 0 \ \wedge \ |F_{att}| \leq FSJ \\ \text{sgn}(F_{att}) \cdot FSJ & se \quad v = 0 \ \wedge \ |F_{att}| > FSJ \\ FDJ & se \quad v \neq 0 \end{cases}$$

Figure 19: Borello friction model equations

The switch that discriminates between static friction and dynamic friction uses the rotation speed of the transmission line $DThSL\ SP$(for the left wing) and $DThSR\ SP$ as a reference value. It should be noted that the value of the $DThSL\ SP$ quantity indicates the value of the speed calculated at the output of the corresponding integrator through the State Port. The value of the quantity provided in State Port is calculated using the value at the previous time step, ignoring the reset condition set by the user for the current integration step. This solution allows the speed value to be used without incurring calculation errors created by the integrator reset condition. In the specific operation of the friction model, the $DThSL\ SP$ value is used to define, in combination with a block that identifies the speed crossing zero, the transition between the static friction and dynamic friction conditions. In general, the State Port value, output from an integrator, must be used exclusively as a control variable for logical-Boolean functional blocks, avoiding the creation of instantaneous feedback loops and the resulting calculation errors in the simulation system. The advantages of using this model implemented with the Saturation Port solution, which is able to correctly simulate end-of-stroke phenomena, compared to the friction models listed above, are considerable both in terms of accuracy and robustness, i.e. the remarkable adaptability to be implemented in complex models with extreme variability of the initial data used.

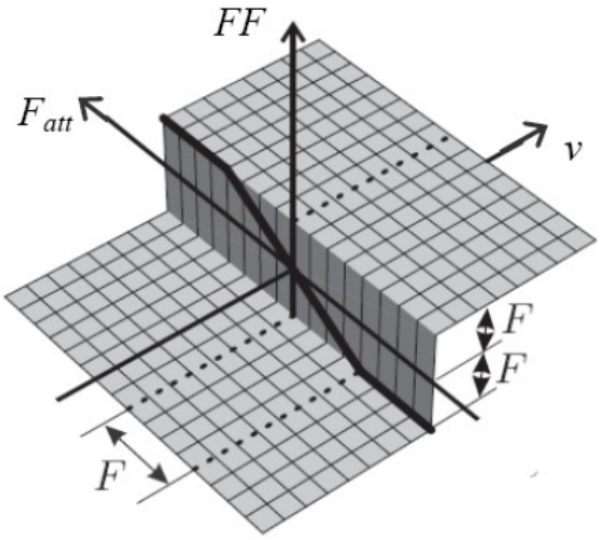

Figure 20: Borello friction model

The results of the comparative tests highlighting these advantages have been omitted from this discussion in order to focus on and summarise the issues and related solutions adopted in the creation of a simulation model for hyper-lift system control.

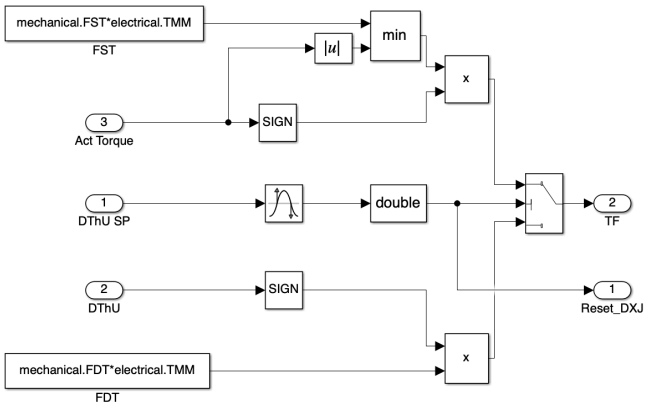

Figure 21: Borello friction model on Simulink

3.2 Irreversibility systems

The use of reversible actuators for moving high-lift surfaces requires the implementation of irreversibility devices for the purpose of:

1. Maintaining the position commanded by the control system;
2. Promptly locking the surfaces in the event of asymmetry associated with a system failure;
3. Limiting the speed of surface retraction with an aerodynamic load configuration favouring motion (aiding load).

For this study purposes the simulations will be only conducted with the implementation of the No-Back Brake device.

3.2.1 Wing-Tip Brakes

The Wing-Tip Brakes (WTB) are located at the end of the kinematic chain consisting of torsion bars. Their location at the end allows the moving surfaces downstream of a break in the motion transmission line to be blocked promptly, reducing the asymmetry resulting from a system failure.

WTBs are multi-disc friction brakes fitted to the end of the transmission line.

In a standard high-lift system configuration, the wing tip brakes are activated hydraulically, which keeps the friction discs of the wing tip brakes spaced apart, allowing the torsion bars to move.

In this simulation, for simplicity, it was decided to maintain the hydraulic supply to the WTBs, identifying as a critical condition, which would require the implementation of this irreversibility system, the sudden loss of electrical power supply.

When the commanded position is reached, obtained by monitoring the transduction sensors, the control system is placed in stand-by, the relief valves are opened and the part of the hydraulic circuit wired to the end brake is deprived of the appropriate pressure. As a result, the coaxial return spring of the friction discs allows them to press against each other, generating a braking torque capable of locking the controlled surface within the acceptable range of the commanded position.

In the event of a failure with loss of part of the mechanical transmission line, the control system, after detecting the asymmetry, performs the same actions as when engaging the WTBs.

Now, a full description of the WTBs is provided for the reader convenience, even if it not applicable for an electromechanical actuation system.

At the same time of the brake engagement, the solenoid valve controlling the hydraulic motor blocks the supply of hydraulic power, and a similar valve system engages another braking system connected to the motor shaft, the POB (Power Off Brake) is engaged, in order to provide adequate rigidity to the entire control system under normal operating conditions and to maintain the controlled surface. As mentioned above, the high aerodynamic load acting on the surfaces free from the mechanical power transmission generated by the system induces enormous acceleration in the direction of the feedback of the components affected by the failure. In conjunction with the continuous controlled movement of the surfaces still under the control of the system, a significant asymmetry in the deployment of the surfaces is generated in a short period of time. Once the failure has been identified, the control system commands the activation of the brake. The delay time with which the brake reacts to the command by locking the surface is a function of certain physical factors, such as the inertia of the components involved and the response

time of the electronic and hydraulic components, which are difficult to modify. The only way to intervene more quickly is to modify the asymmetry monitoring techniques. Among the irreversibility systems under consideration, the WTB solution is the most widely used architecture in civil transport aircraft due to its low cost of implementation and maintenance. Although this solution has longer response times under the same operating conditions, the use of appropriate symmetry control and monitoring systems allows for performance that is entirely comparable to more expensive systems used mainly in the military field, as described below. In addition, WTBs can be tested during the aircraft's pre-flight procedures to assess their operation. In the event of failure due to the high braking torques required to ensure effective braking and the design characteristics of the device with the lowest possible inertia but capable of meeting the operating requirements, the WTB undergoes considerable thermal stress such that it cannot be reused for subsequent flights.

3.2.2 No-Back Brakes

The system in question is the result of the efforts of the Italian company Microtecnica to create a device capable of operating as a band brake in particular load configurations, allowing an irreversibility system to be implemented for each actuator in the control system. The solution adopted is present in numerous flap and slat movement systems for military use, and is in fact used in the following actuation systems:

- Wing Sweep actuation system for TORNADO aircraft;
- Flap-slat actuation system for TORNADO aircraft;
- Flap-slat actuation system for AMX aircraft;
- Slat actuation system for EFA aircraft.

The following figure shows a simplified diagram of the device in question. The moving surface rotates and translates through the connection with the Ballscrew recirculating ball actuator, so the resistant torque applied by the aerodynamic load is applied to shaft 1 through the Millerighe coupling. Shaft 1 ends with a flange shaped to engage the rectangular spring, which is designed to apply a variable braking torque with the difference between the driving torque of the control system and the aerodynamic load. The system that manages the engagement of the flange of shaft 1 consists of the coupling of a shaped cam consisting of surfaces 8 and 10. The spring tension adjustment ring nut 7 allows the torque value at which the locking device intervenes to be set.

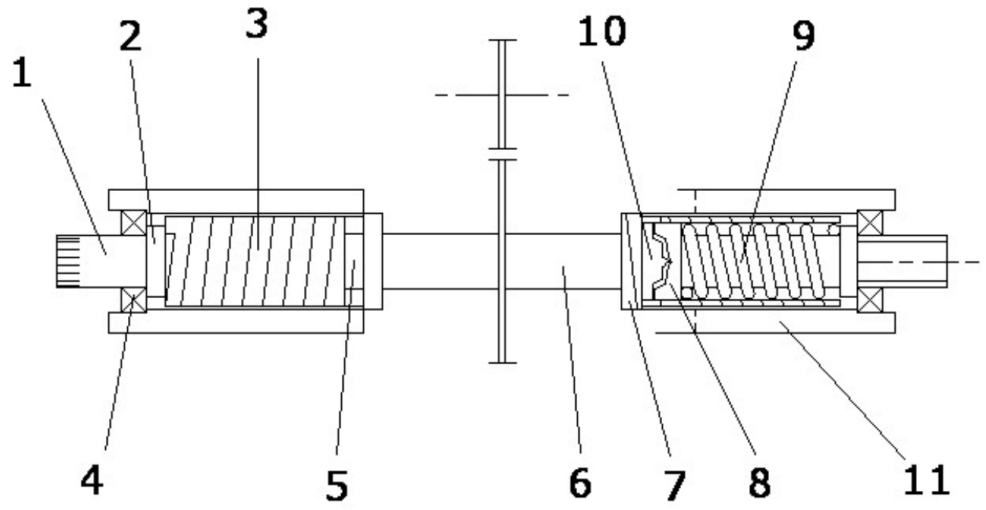

Figure 22: No-Back Brakes scheme

The key parts of the last figure are now presented:

1. Transmission shaft;
2. Anchoring flange;
3. Brake spring;
4. Support bearing;
5. No-Back input shaft;
6. Pinion;
7. Spring tensioning ring nut;
8. Movable cam;
9. Reference torque tensioning spring;
10. Input cam;
11. Structural element.

No-Back Brake working example The diagram in figure 23 shows the position of the adjustment cam in the rest position a. In the rest position, the two shafts exchange pressure forces along surfaces a-a', and the relative positions between the flange of shaft 1 and the brake spring are in a non-engagement condition, as shown in figure 23. In this condition, the brake spring applies a basic static and dynamic braking torque, as a result of being forced into the cylinder that contains it. Since it is not engaged by the flange, it does not apply additional braking torque.

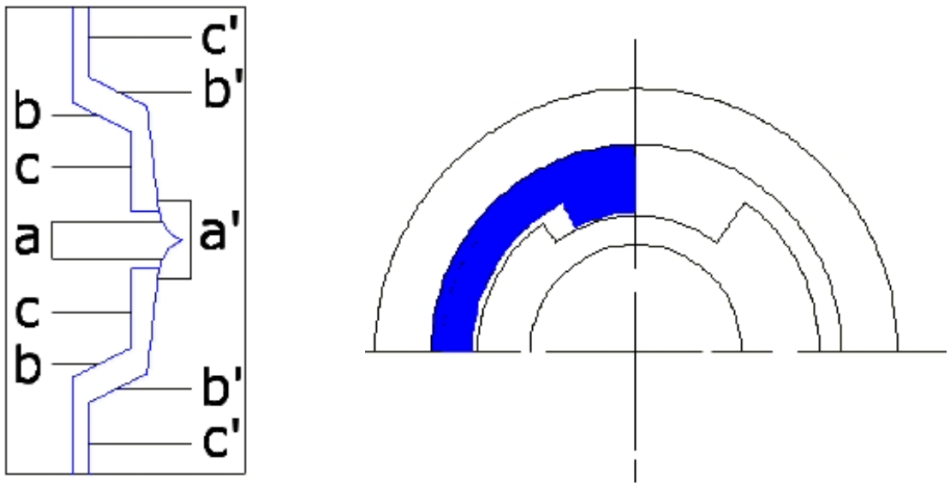

Figure 23: NBB in rest conditions

If the torque differential between the load and the driving torque is different from zero but less than the threshold value defined by the tension imposed on the adjustment spring 9, the cam is positioned as shown in figure 25. In this configuration, shaft 1 exchanges forces with the pinion through the inclined surfaces b-b'. As can be seen from the previous figure, in the relative position between the flange of the shaft connected to the moving surface and the engaging tooth of the brake spring, the engagement angle decreases as the aerodynamic load exceeds the torque delivered by the PDU. Under these conditions, there is proportionality between the intensity of the aerodynamic load and the relative angle for the engagement of the brake spring, the limit of which is given by the adjustment of spring 9, beyond which the spring begins to apply a braking torque proportional to the applied load.

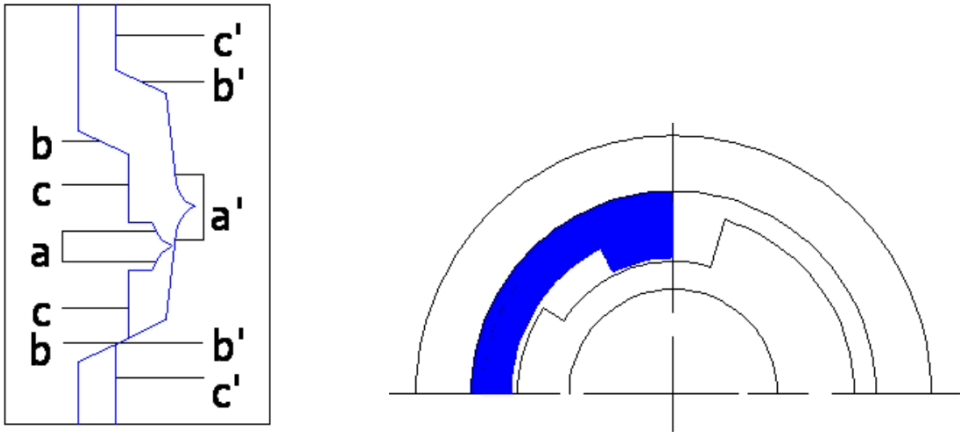

Figure 24: NBB in operative conditions [1]

In the absence of torque delivered by the PDU, the actuators have no input and the aerodynamic loads acting on the moving surface are lower than the reference torque set by spring 9, the cam is positioned in the configuration shown in figure 25. In this configuration, shaft 1 exchanges forces with the pinion through the inclined surfaces b-b'. As can be seen from the previous figure, in the relative position between the flange of the shaft connected to the moving surface and the engagement tooth of the brake spring, the engagement angle decreases as the aerodynamic load increases in comparison with the reference torque of the adjustment spring 9. Under these conditions, there is proportionality between the intensity of the aerodynamic load and the relative angle for the engagement of the brake spring, the limit of which is given by the adjustment of spring 9, beyond which the spring begins to apply a braking torque proportional to the applied load. This condition reflects the normal operation of the high-lift devices when the load does not exceed the maximum torque set by the control system. The No-Back engagement condition is illustrated below, in which the tangential component to the oblique surface of the cam overcomes the friction force and allows the spring to engage. The cam moves to the c-c' coupling conditions shown in Figure 2.15 on page 40, while the shaped flange of the shaft connected to the moving surface engages the tooth of the brake spring, imposing a rotation that increases the friction of the spring on the cylinder wall, thus increasing the braking torque as a function of the relative position between the shaft flange and the spring engagement tooth. The greater the load, the greater the braking torque developed by the spring.

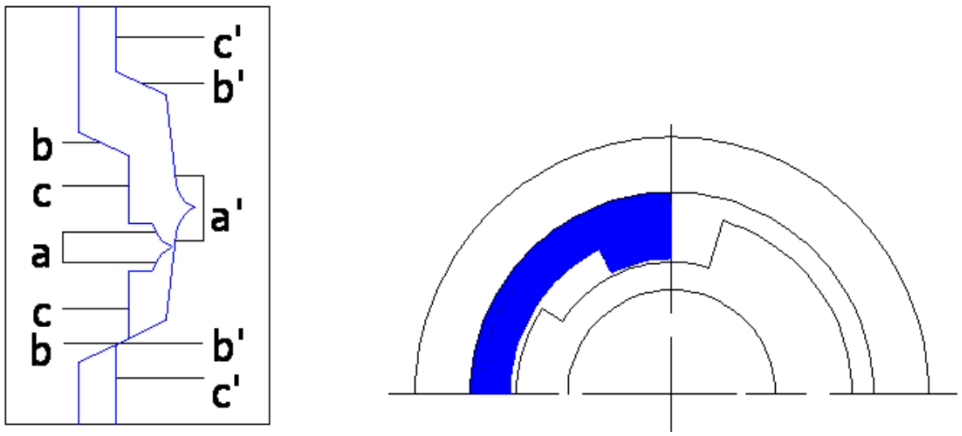

Figure 25: NBB in operative conditions [2]

The difference between the aerodynamic load and the torque provided by the control system is transferred to the moving cam 10. In the case of positive differential, I am in the coupling on the oblique surface. Therefore, the differential can be broken down

into a normal component and a tangential component in the direction of the oblique wall. Both of these forces are applied, with opposite signs, to cam 8, which, unlike cam 10, can move axially. Therefore, the two components applied by cam 10 to cam 8 have an axial resultant that combines with the elastic force applied by adjustment spring 9. Therefore, the two components applied by cam 10 to cam 8 have an axial resultant that combines with the elastic force applied by the adjustment spring 9. When the applied aerodynamic torque generates an axial force on the movable cam greater than the maximum axial force that can be expressed by the spring, the mechanism switches to the relative position between cams c-c', allowing a relative angular position between the drive shaft flange and the tooth for engaging the brake spring 3, which begins to compress its coils, mounted with interference, on the sleeve, developing a considerable braking torque.

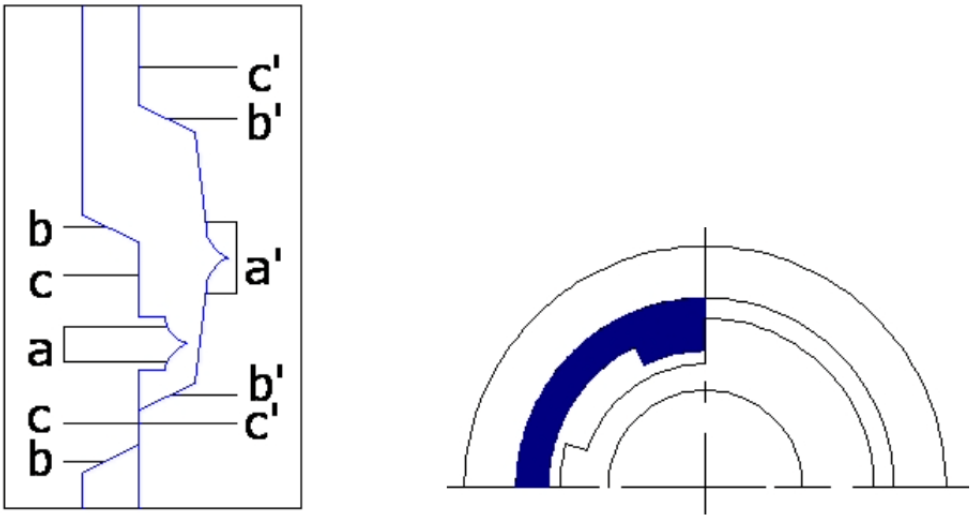

Figure 26: NBB in operative conditions [3]

4 Matlab-Simulink Model

In this chapter the model used in the simulation is going to be presented, with a brief overview on every major component modeled.

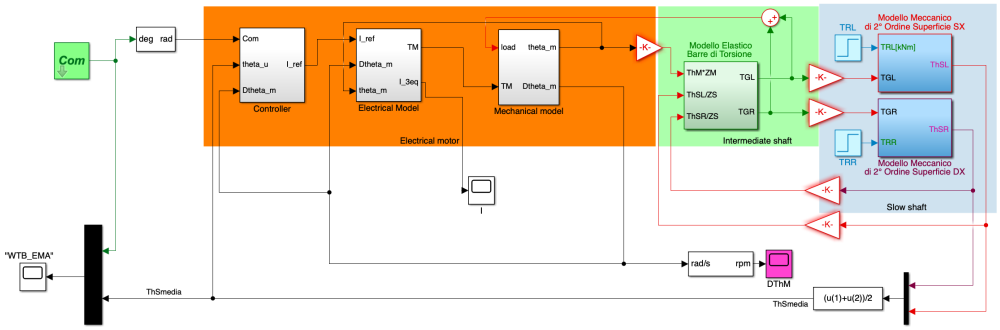

Figure 27: Simulink model

4.1 Electrical motor

In this section is going to be presented the model used in order to simulate the electrical motor, its model is composed by three different blocks, which are the following:

1. Controller
2. Electrical model
3. Mechanical model

4.1.1 Controller

The Controller consists of a proportional control of the error between the desired flap extraction angle and the actual high-lift surface position. The proportional gain that has been utilized is expressed in $\frac{1}{s}$, so the output of this first control is going to be an angular velocity. This quantity is then used to evaluate the angular error by subtracting the actual angular velocity on the moving surface. The angular velocity error is, then, multiplied by another proportional gain, the result obtained is now a current, expressed in A. It is important to note that the two proportional controllers are followed by a saturation block, that limits the angular velocity firstly and lastly limits the current.

The obtained value of current I_{ref} is multiplied by the value generated by the logical asymmetry controller, its logic is explained in section 4.5.

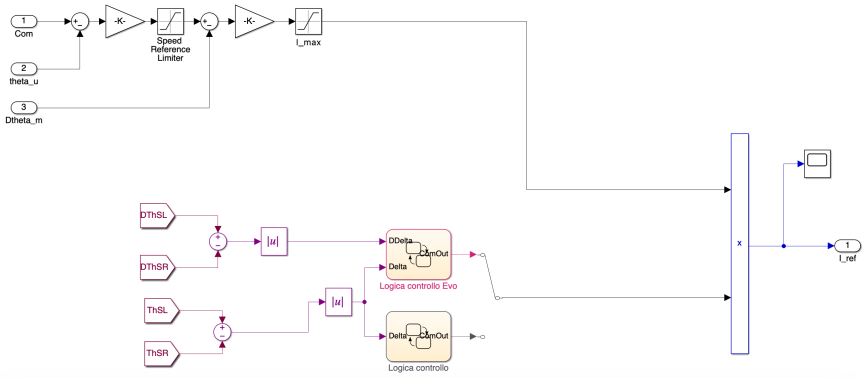

Figure 28: Controller Simulink model

Although more advanced control techniques are available in literature, such as State-space controllers, Fuzzy logic, or Neural Networks, PID (in this case, only a P controller) are still the standard implementation for most industrial and aerospace applications, since they provide better robustness, especially when dealing with significant uncertainties in the behavior of the controlled plant.

4.1.2 Electrical model

The electrical model has been modeled in a low fidelity way that employs an equivalent single phase formulation of the three phases motor. The current setpoint I_{ref} is compared to the actual current flowing in the motor, and a simplified on-off control applies ground or supply voltage to the motor; this is done using a sign block followed by a gain that is equal to the supply voltage of the system V_s . The stator is modeled as a RL circuit, with governing equation:

$$V_m - \Psi(k\omega) = Ri_m + L\frac{d}{dt}i_m \tag{4.1}$$

Where:

- $V_m = V_s$ is the voltage applied to the stator;
- Ψ is the product of two correction factors that will be described in the following paragraph;
- k is the back-EMF coefficient;
- ω is the angular rate of the rotor;
- R is the equivalent resistance;
- L is the equivalent inductance;
- I_m is the current that flows through the motor.

In this way, the supply-to-ground resistance of the motor is preserved, as well as the maximum stator current and RL characteristic time $\tau_F = \frac{L}{R}$. Additionally, this model presents the same current-torque characteristic of an high-fidelity model, by using the same nominal back-EMF coefficient.

The two correction factors are again considered lately in this model in order to obtain the actual torque TMproduced by the electrical motor.

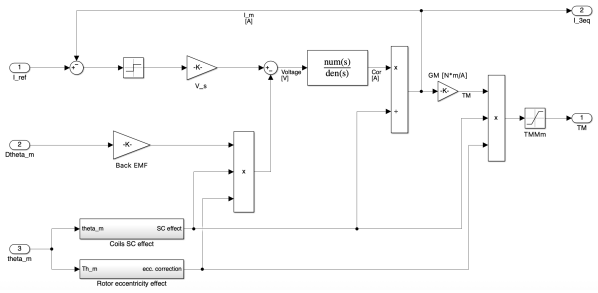

Figure 29: Electrical model on Simulink

Correction factors As said above, two correction factors have been considered in this model in order to correct the next two phenomena:

- Rotor eccentricity;
- Partial short circuit between coils.

Rotor eccentricity is the effect of a misalignment of the bearings supporting the shaft, or of the geometric tolerances of the shaft itself. In general, the axis of rotation of the rotor, the axis of symmetry of the stator, and a principal axis of inertia of the rotor may be slightly offset from each other. The misalignment between the axis of symmetry of the stator and the axis of rotation of the rotor is defined as static eccentricity, while that between the axis of rotation and principal axis of inertia of the rotor is the dynamic eccentricity. This model only considers the static eccentricity that has no immediate effect on vibrations (vibrations are produced by dynamic eccentricity) but can be detected from the ripples produced on currents and voltages of the motor.

Short circuit of the coils is a common failure mode of most electrical machines. In a brushless motor, either PMSM or BLDC, each phase of the stator is manufactured with a number of windings of enameled copper wire. The polymeric coating of the wire is intended to insulate electrically the coils from each other, but has inherently a limited tolerance to high temperature. Occasionally, for example due to unfavorable operating conditions, the maximum temperature for the wire insulation may be exceeded, resulting in the short circuit of a coil with the next one.

4.1.3 Mechanical model

The mechanical model of the motor and transmission computes the positions of motor and user, receiving as an input the motor torque and the external load torque. The core of the model is a second order dynamical characterization of the system, described by the equation:

$$TM - T_{LOAD} = J_m \frac{d^2}{dt^2}\theta_m + C_m \frac{d}{dt}\theta_m \tag{4.2}$$

Where:

- TM is the torque produced by the motor;
- T_{LOAD} is the torque load of the system;
- J_m is the inertia of the system;
- C_m is the viscous friction coefficient of the system, which, in this case, is considered steady;
- θ_m is the angular position of the motor shaft;

In addition, the model accounts for a number of non-linear phenomena affecting the behavior of the actuators, such as endstops, friction, and backlash.

The collision with endstops is detected by a saturated position integrator. When a saturation is detected, the following actions are performed:the velocity integrator is reset to zero and if the total torque acting on the system is aligned with the endstop (i.e. pushes the actuator against the endstop), it is overwritten to zero.

The friction is modeled with the Borello friction model that is already presented in section 3.1.7

To summarise, this block calculates the angular position θ_m and velocity $\dot{\theta}_m$ of the motor shaft (also known as fast shaft) starting from its two inputs, the torque produced by the motor TM and the load torque T_{LOAD}.

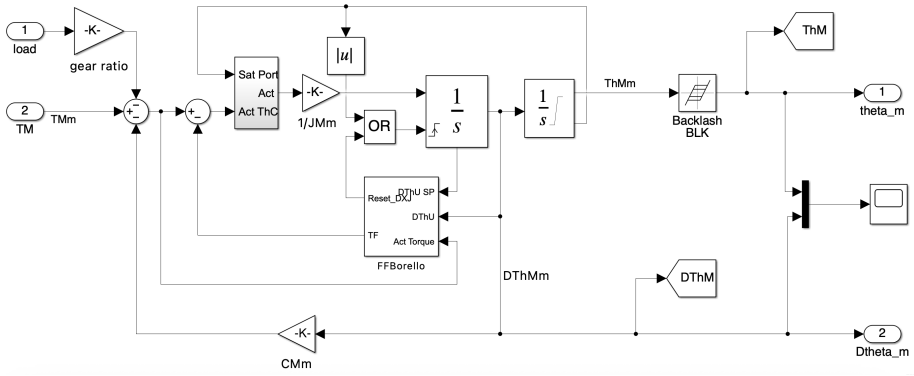

Figure 30: Mechanical model on Simulink

4.2 Transmission of motion via shafts

Motion is transmitted through the use of a series of elements that have elastic flexibility in the kinematic coupling between the variuos elements.

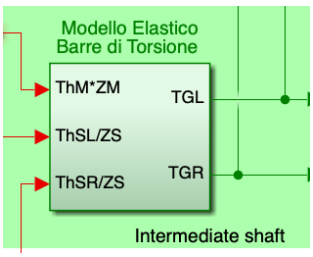

Figure 31: Intermediate shaft block

In addition, the transmission line has reducers that allow the number of revolutions per minute to be decreased, starting from the electric motor shaft identified as the fast shaft and ending the kinematic chain with the surface actuator unit identified as the slow shaft. Between the two main reduction gears, there are torsion bars interconnected by couplings and brackets, identified as the middle shaft. For simplicity, the simulation model has a single torsion bar between the first and second reduction gears for each wing of the aircraft.

Identifying the three main components of the kinematic chain in the manner described above allows references to be made by reporting angular quantities and torques transmitted to a common shaft so that they can be compared or simply used in the algebraic relationships provided by the mathematical model.

The transmission ratios used in the model are identified with the parameters ZM and ZS.

In the representation of the basic transmission line model, the coupling clearances were considered using the BLG parameter, which refers exclusively to the final actuator, whose value can be differentiated according to the wing half considered by introducing a value in the BLGL (left half-wing) and BLGR (right half-wing) parameters.

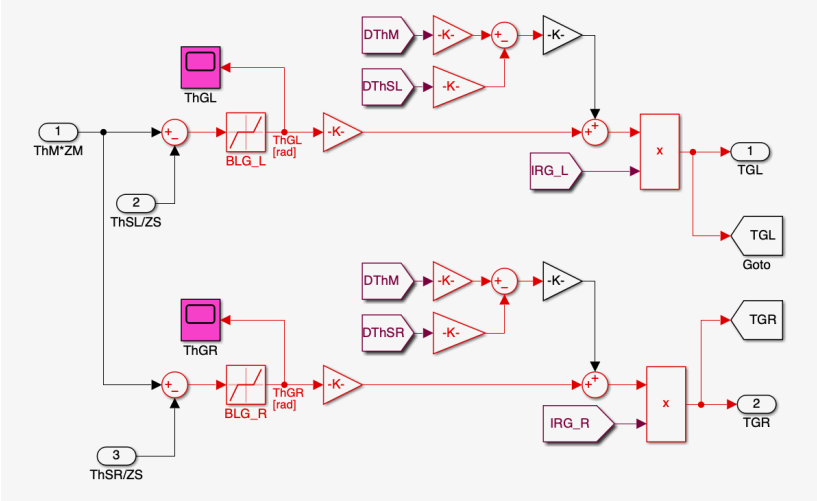

Figure 32: Intermediate shaft model on Simulink

The angle of deformation of the transmission line is represented by the following equation:

$$\theta_{trasm} = \theta_m Z_m - \frac{\theta_S}{Z_S} - + BLG \tag{4.3}$$

Except for the dead band represented by the condition:

$$\theta_{trasm} = 0 \tag{4.4}$$

$$-BLG <= \theta_{trasm} <= BLG \tag{4.5}$$

The torque transmitted by the transmission system consists of the following components:

$$C_{trasm} = IRG(C_{elast} + C_{visc}) \tag{4.6}$$

$$C_{elast} = KG\theta_{trasm} \tag{4.7}$$

$$C_{visc} = CG\dot{\theta}_{trasm} \tag{4.8}$$

$$\dot{\theta}_{trasm} = (\dot{\theta}_m Z_m - \frac{\dot{\theta}_S}{Z_S}) \tag{4.9}$$

It should be noted that the IRG parameter, which appears in the dynamic equilibrium formula of the torsion bar, represents the failure of the transmission bar itself, assuming a value of zero. During normal operation, the bar failure variable is set identically to one in order to simulate the kinematic continuity of the transmission line.

The Simulink block calculates the TGL and TGR torques for each half-shaft using elastic clearances and deflections and visco-elastic damping coefficients.

These torques, corresponding to the transmitted torque identified in the mathematical model with CTrasm, represent the output input variables to the simulation block inherent to the final actuator and the surface These torques, corresponding to the transmitted torque identified in the mathematical model with CTrasm, represent the input variables to the simulation block related to the final actuator and the moving surface it moves.

4.3 Slow shaft and actuation

In the section dedicated to the transmission model, the driving torque (TGL and TGR) was calculated for each wing half applied to the actuator input.

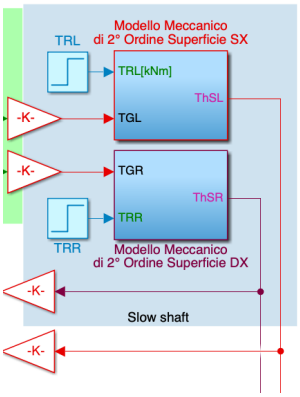

Figure 33: Actuation model blocks

In this model, the actuator and the moving surface mechanically connected to it are considered to be free of elastic deflections and constructional clearances, analogous to the behaviour of a rigid body whose dynamics are defined by the behaviour of a second-order model analogous to the mass-spring-damper model.
The quantities calculated in other simulation blocks will all be reported in the slow shaft through the characteristic ratio of the last reduction stage. The following quantities will be considered in the calculation of the dynamic equilibrium equation:

- CDisp: torque available from the hydraulic motor through the kinematic line, indicated in the model by the quantity TGL for the left wing and TGR for the right wing.
- CVisc: viscous damping torque proportional to the rotation speed of the moving surface. This contribution considers damping phenomena mainly associated with the actuator.
- CEst: torque external to the flap movement system, representing the torque of the resistant hinge in the model represented by the quantity TRR , for the load on the right wing, and TRL for the aerodynamic load acting on the left wing.
- CIrrev: braking torque generated by the irreversibility device used in the overall model. This contribution is added to that expressed by the friction model as described in the relevant section on Irreversibility Systems.
- CAttr: braking torque of the friction model, whether static or dynamic.
- CIn: overall inertia torque of the surface actuator block considered as a single equivalent rigid body.

$$C_{disp} + C_{In} - C_{Visc} - C_{Attr} - C_{Irrev} - C_{Est} = 0 \tag{4.10}$$

Where:

$$C_{disp} - C_{Visc} - C_{Est} = Act \tag{4.11}$$

$$C_{Attr} - C_{Irrev} = C_{Res} \tag{4.12}$$

$$Act - C_{Res} + C_{In} = 0 \tag{4.13}$$

Considering the position, velocity and acceleration of the moving surface as $\theta_s \dot{\theta}_S \ddot{\theta}_S$ is possible to re-write the dynamic equilibrium equation actors in the following way:

$$C_{Visc} = CS\dot{\theta}_S \tag{4.14}$$

$$C_{Est} = C_{Est_k} + TR_\theta \theta_S \tag{4.15}$$

This contribute is composed by a costant value and a variable part which is function of the angle of the moving surface.

$$C_{Disp} = \frac{C_{Trasm}}{Z_S} \tag{4.16}$$

$$C_{In} = -J_S \ddot{\theta}_S \tag{4.17}$$

From the last equation is possible to obtain the following:

$$\dot{\theta}_S = \frac{Act - C_{Res}}{J_S} \tag{4.18}$$

(4.19)

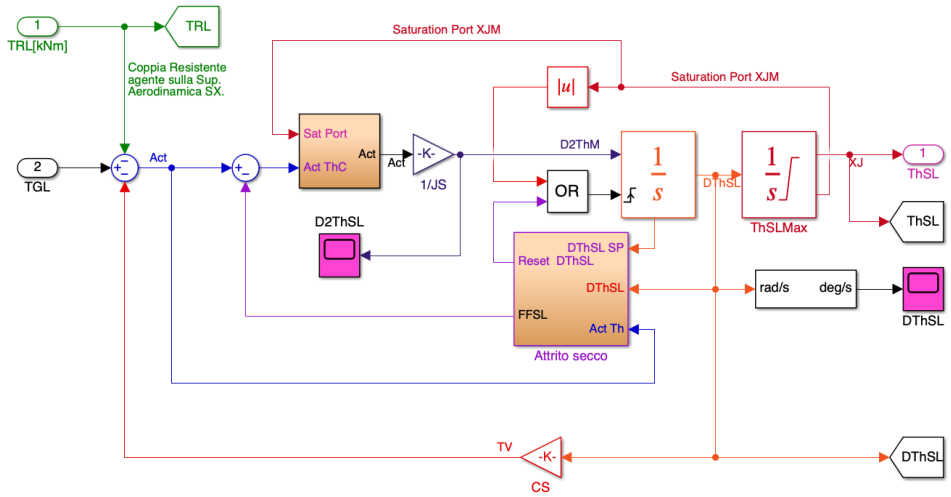

Figure 34: Actuation model on Simulink for an half-wing

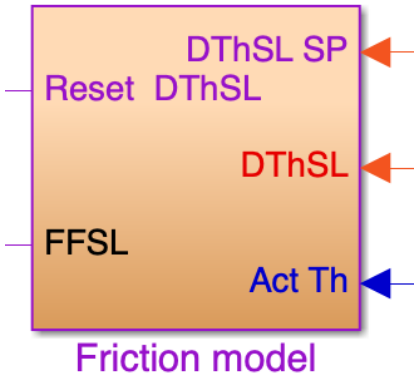

Figure 35: Friction model overview

Friction model is composed of a classical Borello friction model, as described in the 3.1.7 section with the implementation of the No-Back Brake device which is now presented.
The braking contribution of the No-Back device, whose mathematical model is described in the 3.2.2 section, is implemented within the friction model by adding its value to both the static friction value and the dynamic friction value using an appropriate scale factor. The scaling factor represents the ratio between the static friction value and the dynamic friction value, and has been set to two in reference to the type of contact between the brake spring and the cylinder of the No-Back device. The implementation of the block that simulates the behaviour of the No-Back system within the proposed friction model is represented by figures 35 and 36.

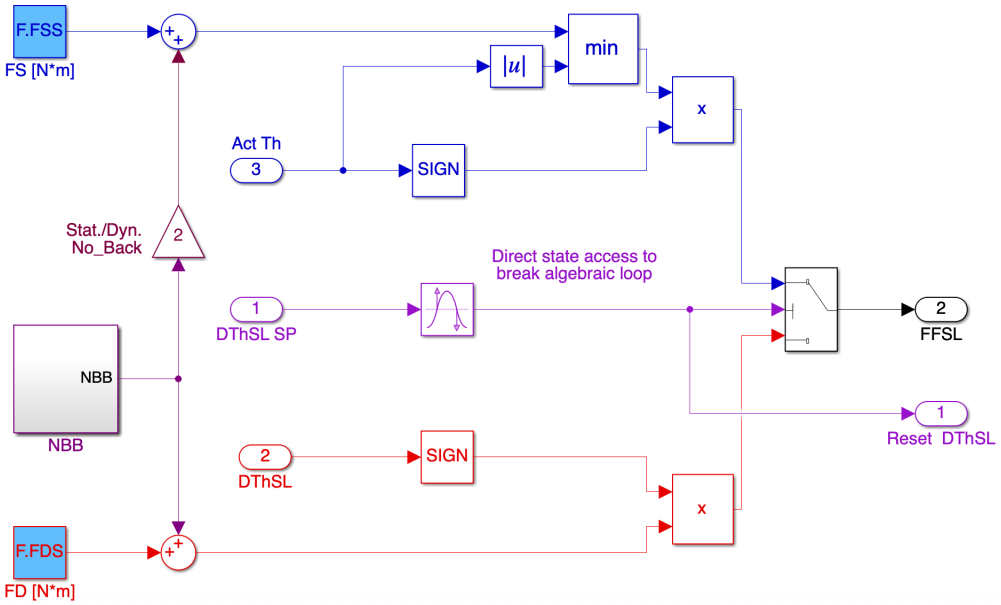

Figure 36: Friction model

The simulation block calculates the value of the braking torque FF_{NoBack} using the input variables TGL and TRL, which represent the value of the driving torque transmitted to the shaft and the value of the resistant torque applied to the moving surface of the left wing half, respectively. The contribution of the braking torque FF_{NoBack} is added to the torque resulting from the friction actions corrected with an appropriate scale factor depending on the type of friction (static or dynamic) to which it is added. An identical simulation solution was implemented for the right wing transmission line in order to differentiate the calculation conditions and dynamic behaviour of the two wings, allowing the simulation of a wide variety of operating conditions that are not necessarily symmetrical. Within the No-Back simulation block (figure 37), the variable $\Delta TG = |TGL| - |TRL|$, the input value of the Lookup Table, which represents the relationship between 37), the variable ΔTG and FF_{NoBack} by points, is calculated by subtracting the respective absolute values from the input quantities.

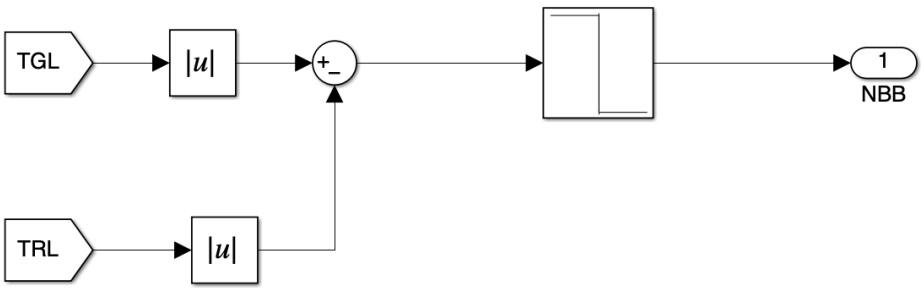

Figure 37: No-Back Brake model

The approximate relationship between the braking torque generated by the irreversibility device and the difference between the driving torque available at the No-Back input and the hinge torque acting on the moving surface is shown in figure 38.

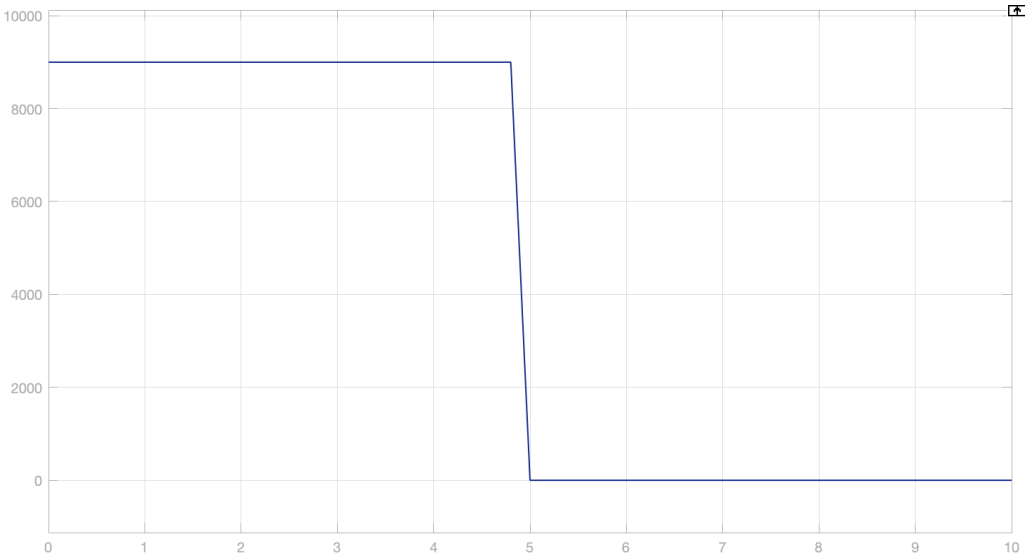

Figure 38: No-Back Brake lookup table

Although approximate, this relationship describes the specific characteristics of the No-Back drive. In fact, when the driving torque equals or exceeds the resistant torque of the resultant of the aerodynamic forces acting (ΔTG), the device provides an additional contribution to the friction force, approximated to the previously calculated value of 10 Nm. This braking contribution is always applied in dynamic conditions to the transmission line, both in aiding load conditions and in opposing conditions, and is a function of the interference torque with which the braking spring is assembled to the cylinder. This braking contribution is always applied in dynamic conditions to the transmission line, both in aiding and opposing load conditions, and is a function of the interference torque with which the brake spring is assembled to the device cylinder.

At the moment when the resistant torque exceeds the driving torque in modulus, the braking torque generated by the No-Back increases linearly with the value of ΔTG up to the maximum value. The maximum braking torque that can be delivered by a single NBB device is capable of sustaining the maximum aerodynamic load applicable under operating conditions, considering a safety factor of 1.5.

It should be noted that the maximum braking torque developed refers to a single No-Back system. In the overall architecture of the movement system, at least two braking devices are provided for each of the moving surfaces in order to prevent skewness, i.e. asymmetrical extraction in the directional plane of the aircraft for each individual surface. Therefore, the combined action of two NBB devices ensures safe locking of the aerodynamic surface affected by the failure under any aerodynamic load condition. The creation of more accurate simulation models to describe the operation of NBB brakes, using an approach based on the angles of engagement between the shaped cam shaft and the brake spring tooth inside the device, makes the system sensitive to changes in the initial data entered. This sensitivity results in simulation behaviour that does not correspond to experimental reality. The proposed model uses a torque approach, which allows for a seemingly simpler solution but with considerable robustness to variations in the simulation data entered.

4.4 Aircraft dynamical model

In order to evaluate the effects of asymmetry during the movement of the movable high-lift surfaces, a block of instructions was introduced into the simulation model to approximately represent the roll dynamics of the reference aircraft used to define the parameters of the simulation architecture. The model representing the roll dynamics of the entire aircraft was developed in an extremely simplified manner in order to capture the behaviour of the roll dynamics alone, neglecting the effects of coupling with the other dynamics of aircraft motion. The simplified roll dynamics model consists of four distinct blocks of instructions, each simulating a specific aspect of the dynamics under analysis:

- Aerodynamic Torques Model: This block of instructions calculates the aerodynamic torques acting on the aircraft's longitudinal axis XBody, based on the deflection angles of the moving surfaces and the aircraft's speed.
- Dutch Roll Model: simplified model of the aircraft's roll dynamics analogous to the dynamics of a second-order system expressed in Laplace variables, in which the yaw coupling effects associated with roll motion are neglected;
- Autopilot: simplified model of the actions of an autopilot which, in analogy with a PID controller, processes control actions capable of counteracting the effects of the roll model associated with the asymmetry of the extraction of the high-lift surfaces;
- Aileron Control Model: the control actions processed by the autopilot model are translated by this simulation model into aileron deflection angles in order to compensate for the roll induced by the extraction asymmetry. The deflection angle processed is a saturated quantity in position and speed.

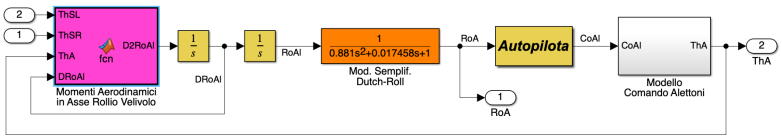

4.4.1 Aerodynamics torque model

In this block are modeled the following equations:

$$MRF = \frac{\rho}{2} TAS^2 \frac{ThSL - ThSR}{2} \tag{4.20}$$

$$MRA = \frac{\rho}{2} TAS^2 ThA \tag{4.21}$$

$$MRP = \frac{\rho}{2} TAS^2 DRo \tag{4.22}$$

$$D2Ro = \frac{MRF + MRA - MRP}{J_{xx}} \tag{4.23}$$

Where:

- MRF is the roll torque due to flap assimetry;
- MRA is the roll torque due ailerons deflection;
- MRP is the damping torque due to roll velocity;
- D2RoAl is the roll acceleration.

4.4.2 Dutch-Roll model

In this block a simplified dutch-roll model is implemented in a second order dynamic, ignoring the coupling effects between the Longitudinal and Latelar-Directional Plane of the aircraft.

4.4.3 Autopilot model

In this block a PID controller acts as an autopilot using as an input the roll angle and the aileron command is obtained as a result.

The working principles of a PID controller are described in section 2.7

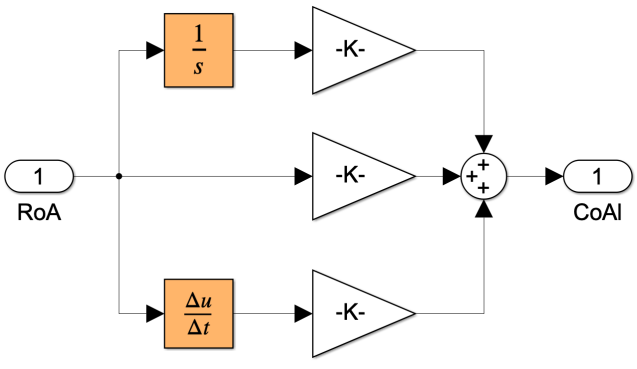

Figure 39: Autopilot model

4.4.4 Aileron control model

In this block a second order dynamic is implemented in a way to simulate ailerons' actuation after having received the autopilot command, to keep an higher level of fidelity the output is limited (saturated) both in position and in velocity.

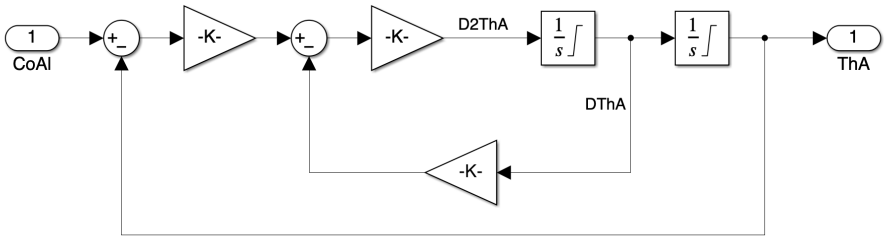

Figure 40: Aileron model

4.5 Control logics

The monitoring technique implemented in this model involves the use of both the difference in angular position between the two kinematics $\Delta\theta$ and the difference between the actuation speeds $\Delta\dot{\theta}$ of the two kinematic lines relating to the half-wings. The logical architecture involves controlling the differential speed when a predefined threshold is exceeded in order to activate a warning condition, which can evolve into the activation of the emergency stop protocol when the angular differential threshold is exceeded. The time counter increases or decreases in relation to the speed threshold being exceeded, as this occurs well before the angular threshold is exceeded. However, the advancement of the counter in the event of the speed threshold being exceeded allows a maximum level to be reached equal to the characteristic fault recognition time, which differs from the final time limit, for a smaller number of time steps than the initial zero reference. When the angular differential reference threshold is exceeded, the characteristic time threshold is exceeded, activating the shutdown procedure.

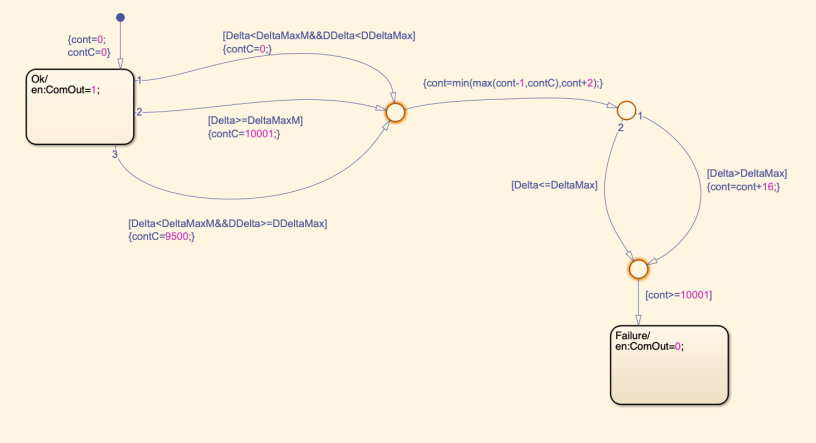

Figure 41: Control logics

5 Simulation

5.1 Simulation cases

For this thesis' purposes the following operating cases have been analyzed and simulated:

- Flap actuation to a 10 degrees extraction;
- Flap actuation to 40 degrees extraction;
- Flap retraction from a 10 degrees position;
- Flap retraction from a 30 degrees position;

For each case were conducted three different simulations:

- Nominal condition;
- Failure with the control logic implemented;
- Failure without the control logic implemented;

The failure condition implemented in the model consists in a break of the intermediate shaft that implicates the total loss of the mechanical power transmission, thus the high-lift surface cannot be controlled by the pilots anymore. The failure in applied approximately at the moment of the half extraction or retraction of the surfaces.

For each of the simulation case in the next sections are going to be presented five different graphs as follows:

- The command and the average extraction of the surfaces in the nominal condition;
- The command, the average extraction of the surfaces and the extraction of each surface in the failure condition with the control logic implemented;
- The aileron deflection angle in the same conditions;
- The command, the average extraction of the surfaces and the extraction of each surface in the failure condition without the control logic implemented;
- The aileron deflection angle in the same conditions;

5.2 Flap actuation to a 10 degrees extraction

This first simulation was conducted in order to validate the entire model. Only a 10 degrees step command had been applied to the system after a period of 0.1 seconds from the beginning of the simulation.

5.2.1 Nominal case

In this figure is possible to note that the flap surfaces are extracted to the correct and desired position in a reasonable amount of time, around three seconds. This result is compliant with the requirements that are usually imposed for the flap extraction.

After reaching the commanded position the surfaces are able to maintain the degree of extraction counterbalancing the aerodynamic forces and moments to which the system is subjected.

Is also important to make clear that the logical control of the flap extraction is implemented in this simulation case, but has only a monitoring function since no failures are detected or imposed to the flap actuation system.

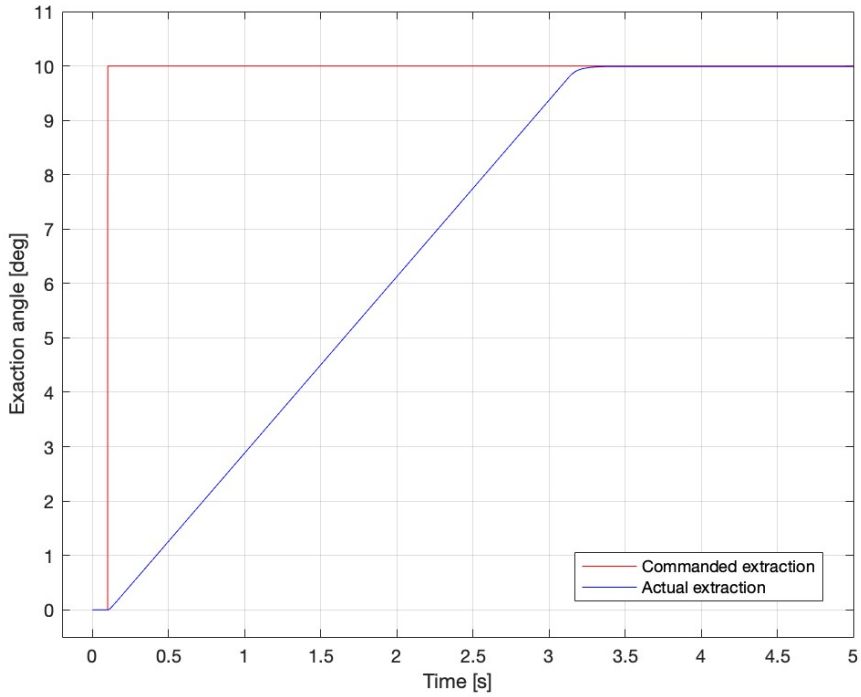

Figure 42: Flap extraction to 10 degrees

5.2.2 Failure with the control logic implemented

In this case the simulation has been done with a failure that occurs after 1.5 seconds of actuation. Both of the surfaces had reached the position of approximately 4.5 degrees at the time of the failure. After the failure the left surface is left without moving torque, so the No-Back Brake implemented in the left half-wing starts working in order to stop the surface from retraction under the aerodynamic forces and moments, thus the surface is blocked at 4.5 degrees. Immediately after the left surface stopped its motion the control logic notes that and starts a compensating action in order to mitigate the actuation asymmetry, once the maximum possible difference between the two extraction positions the control logic commands also the stop of the right surface extraction. Around 0.2 seconds after the failure the actuation is completely stopped.

In collaboration with the control logic, that mitigates the consequences of the power transmission line failure, the ailerons motion is commanded by the autopilot with the purpose of compensating the roll angle that is caused by the flap asymmetry.

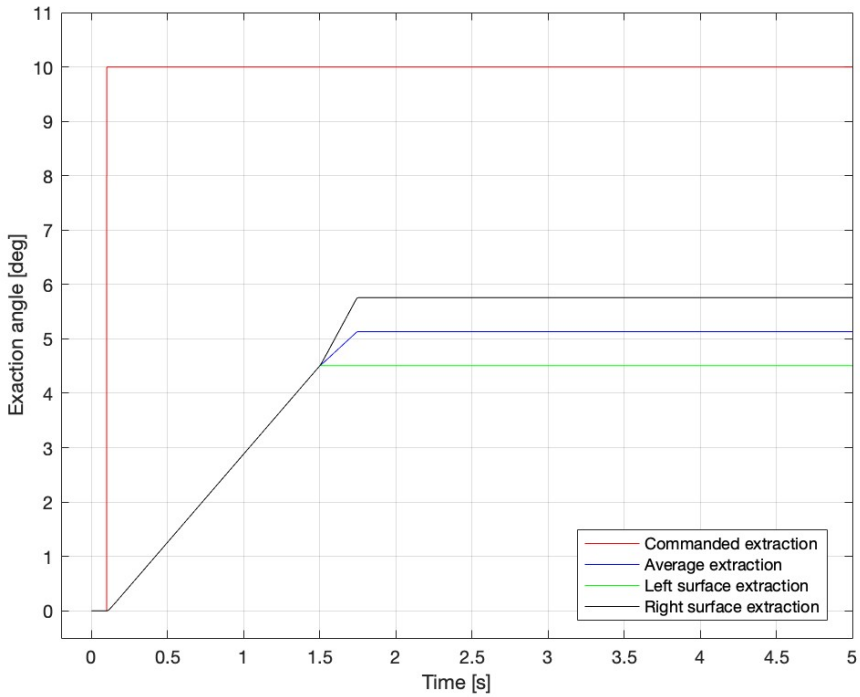

Figure 43: Flap extraction to 10 degrees with failure and controller

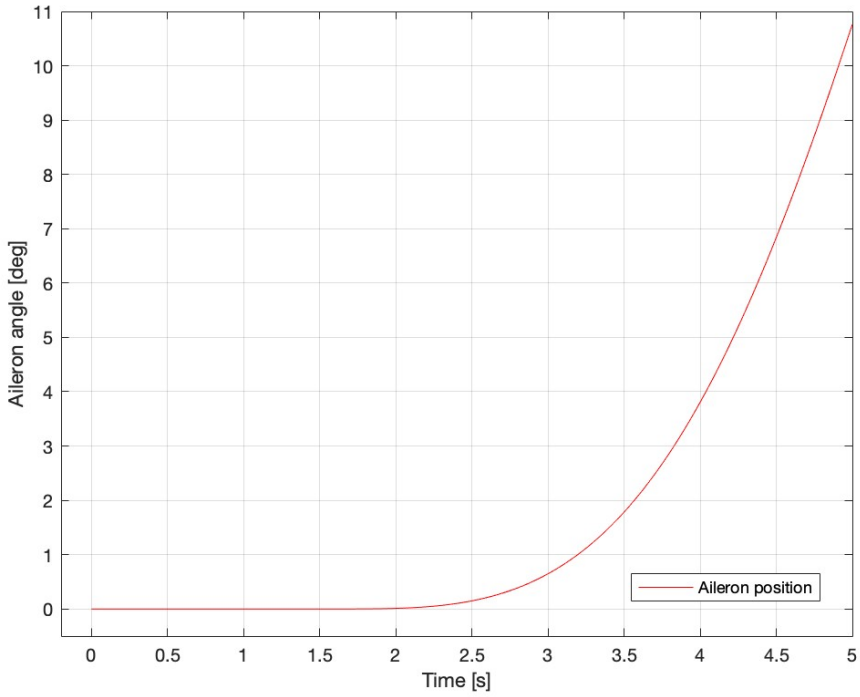

Figure 44: Aileron behavior

5.2.3 Failure without the control logic implemented

The simulation is conducted in the similar way of the latter. In the model used for this particular case the control logic was turned off, so no flat asymmetry control and mitigation is performed by the flap actuation system. After the failure that occurs, again, at 1.5 seconds from the beginning of the actuation the left surface movement is of course blocked by its No-Back Brake. Given the fact that the control logic is not working in this simulation case the right surface continues to be extracted. In this specific case we can note that the average flap surfaces position reaches the commanded extraction while the right surfaces reaches an higher extraction, this is a modeling issue because the controller of the motor has as an input the average position of the two surfaces and not the position of each surface due to the non-distributed architecture of the system. It is possible to note that the ailerons are fully extracted in a very short period of time and they have reached the maximum limit of 25 degrees without having compensated the flap asymmetry.

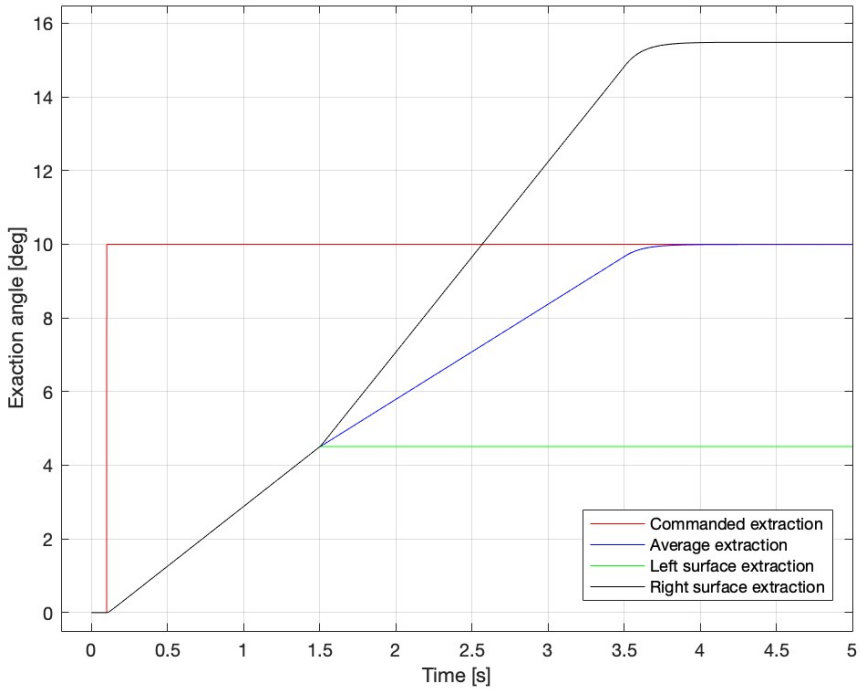

Figure 45: Flap extraction to 10 degrees with failure and no controller

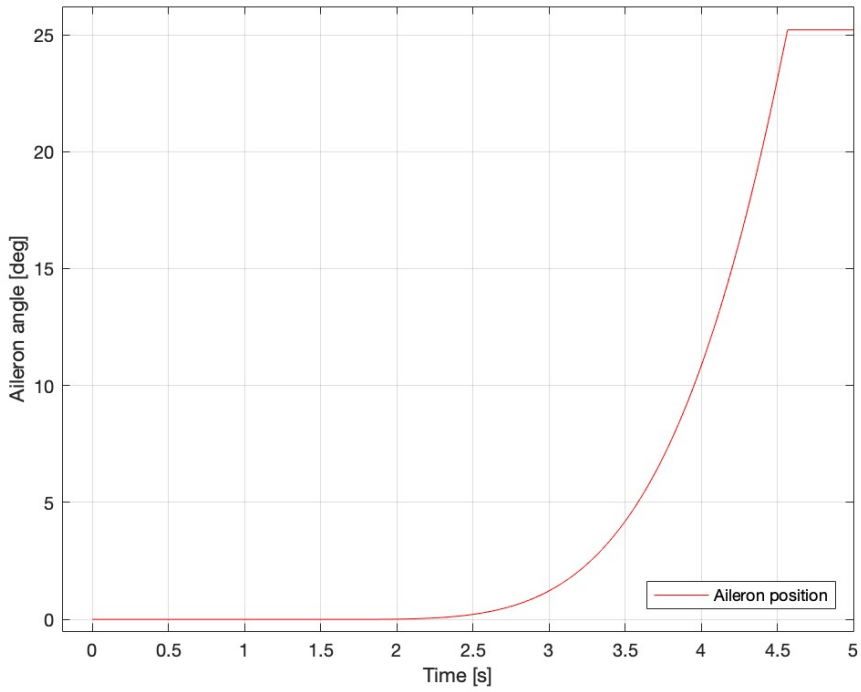

Figure 46: Aileron behavior

5.3 Flap actuation to 40 degrees extraction

In this simulation case a almos full extraction of the high-lift surfaces is commanded, a 40 degrees extraction is requested to the actuation system.

5.3.1 Nominal case

In this figure, it can be observed that the flap surfaces are deployed to the correct and desired position within a reasonable timeframe — approximately 13 seconds. This performance meets the typical requirements established for flap deployment.

Once the commanded position is reached, the surfaces are able to maintain the specified level of extension, effectively counteracting the aerodynamic forces and moments acting on the system.

It is also important to note that while the logical control for flap deployment is implemented in this simulation, it functions solely in a monitoring capacity, as no faults are detected or introduced in the flap actuation system.

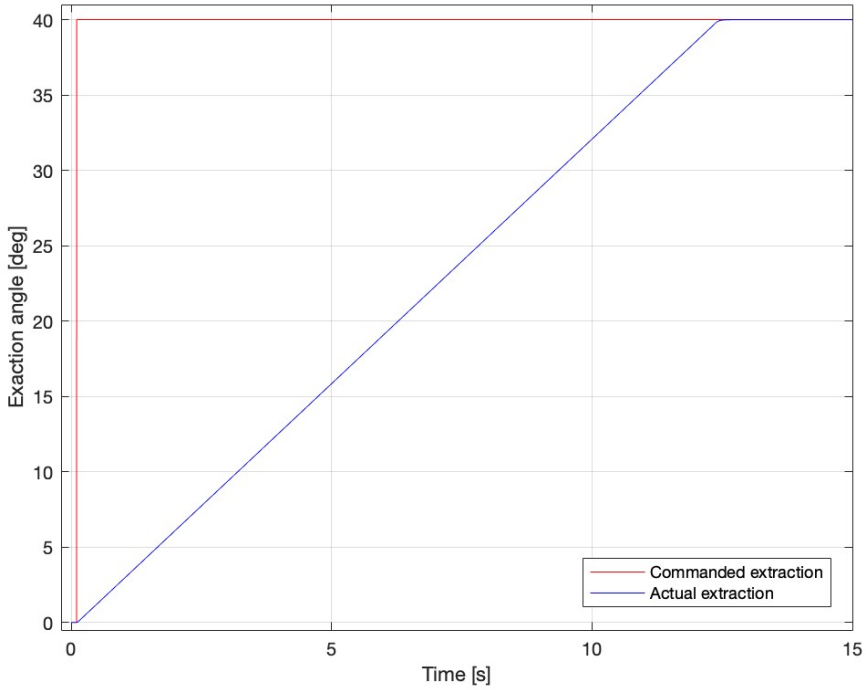

Figure 47: Flap extraction to 40 degrees

5.3.2 Failure with the control logic implemented

In this scenario, the simulation includes a failure that occurs 6.5 seconds after the start of actuation. At the moment of the failure, both surfaces had reached an angle of approximately 21 degrees. Following the failure, the left surface loses its actuation torque. As a result, the No-Back Brake installed on the left half-wing engages to prevent retraction due to aerodynamic forces and moments, effectively locking the surface at 21 degrees.

Immediately after the left surface ceases movement, the control logic detects the issue and initiates a compensatory action to reduce the resulting actuation asymmetry. Once the maximum allowable difference between the two surface positions is reached, the control system also commands the right surface to stop. As a result, the actuation process is fully halted approximately 0.2 seconds after the failure occurs.

In coordination with the control logic, which mitigates the impact of the power transmission failure, the autopilot commands aileron movement to compensate for the roll moment induced by the flap asymmetry.

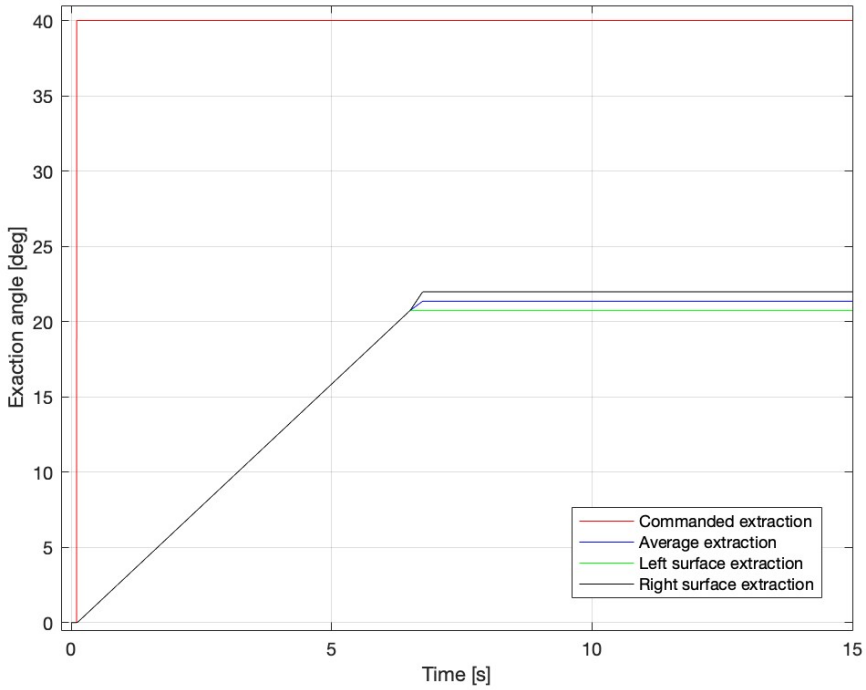

Figure 48: Flap extraction to 40 degrees with failure and controller

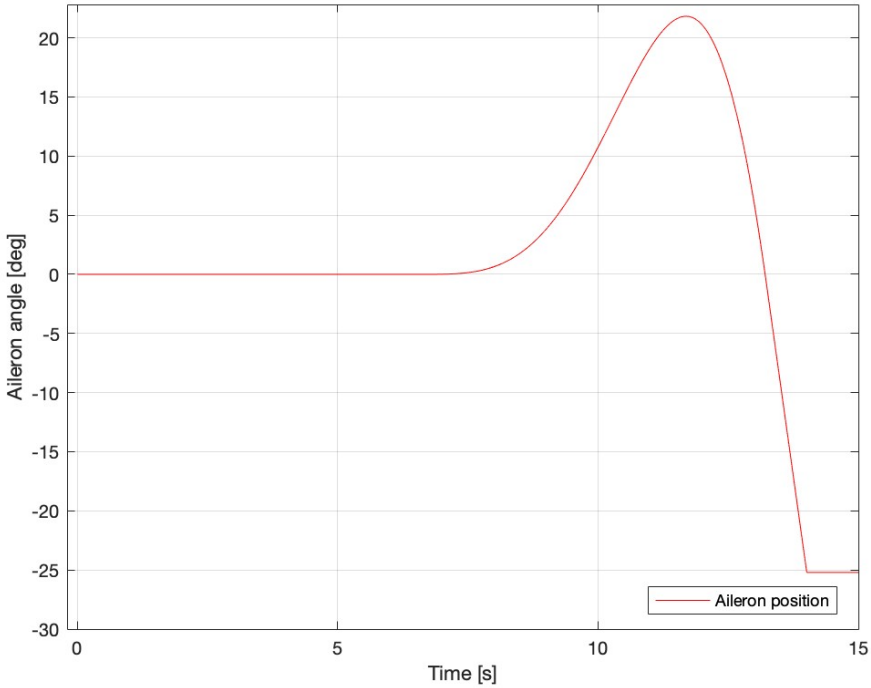

Figure 49: Aileron behavior

5.3.3 Failure without the control logic implemented

This simulation is conducted in a similar manner to the previous case. However, in this particular scenario, the control logic is disabled, meaning the flap actuation system does not perform any asymmetry control or mitigation.

As in the earlier case, a failure occurs 6.5 seconds after the start of actuation, causing the left surface to be locked by its No-Back Brake. Since the control logic is inactive, the right surface continues its movement uninterrupted.

In this scenario, the average flap position reaches the commanded extraction value, while the right surface alone exceeds it. This discrepancy highlights a modeling limitation: the motor controller uses the average position of both surfaces as input, rather than individual surface positions, due to the system's non-distributed architecture.

It can also be observed that the ailerons are fully deflected in a very short time, reaching their maximum limit of 25 degrees, without effectively compensating for the flap asymmetry.

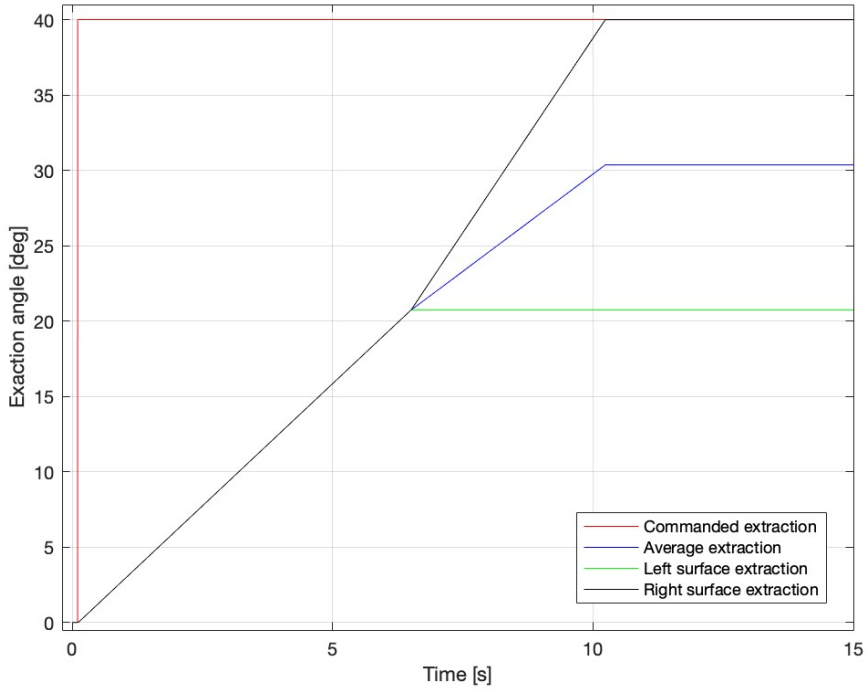

Figure 50: Flap extraction to 40 degrees with failure and no controller

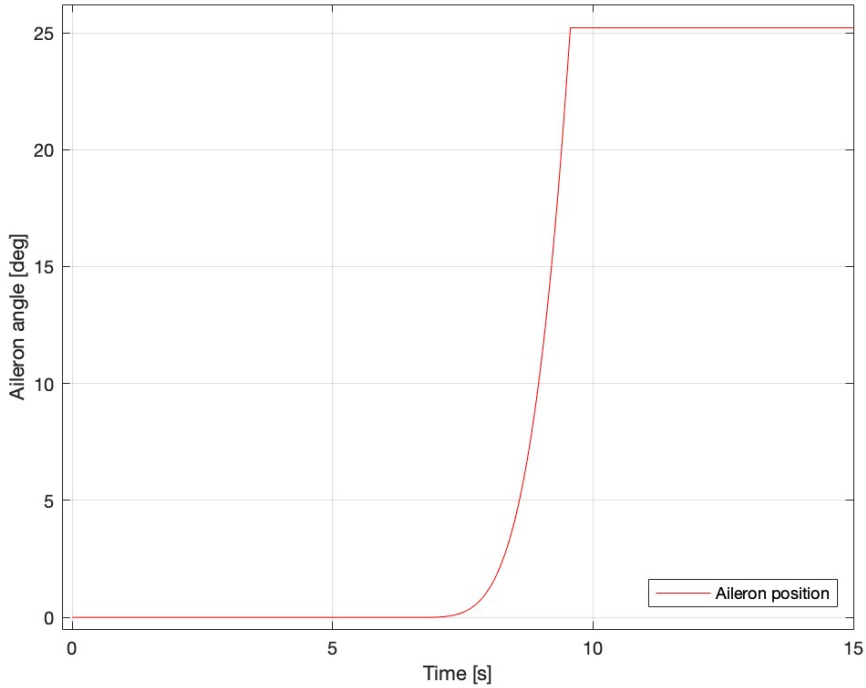

Figure 51: Aileron behavior

5.4 Flap retraction from a 10 degrees position

This simulation case intends to verify if the system could retract the flap surfaces from an operative condition. The retraction is simulated with a prior extraction in order to maintain the highest degree of compliance with the standard operations. In this particular case the extraction and retraction requested to the system is equal to 10 degrees.
The plots that are shown in this section report only the retraction phase of the simulation because the extraction has already been verified in the previous sections.

5.4.1 Nominal case

In this plot the nominal case of the simulation is reported, it is notable that the surfaces are in a 10 degrees extraction position at the beginning of the simulation and then a 10 degrees retraction is commanded to the flap actuation system. The retraction is performed in a little amount of time: around 2.5 seconds. This result is compliant with the requirements that are usually imposed for the flap extraction. This period of time is shorter than the one needed for the extraction at a 10 degrees position, this is due to the aerodynamic loads that now are in a aiding condition. An aerodynamic load is in an aiding condition when the relative forces and moments are helping the system moving in the way that is commanded. An opposing aerodynamic load is a force or a moment that is resistant the moving torques imposed by the motors or the mechanical power sources. Is important to make clear that the logical control of the flap extraction is implemented in this simulation case, but has only a monitoring function since no failures are detected or imposed to the flap actuation system.

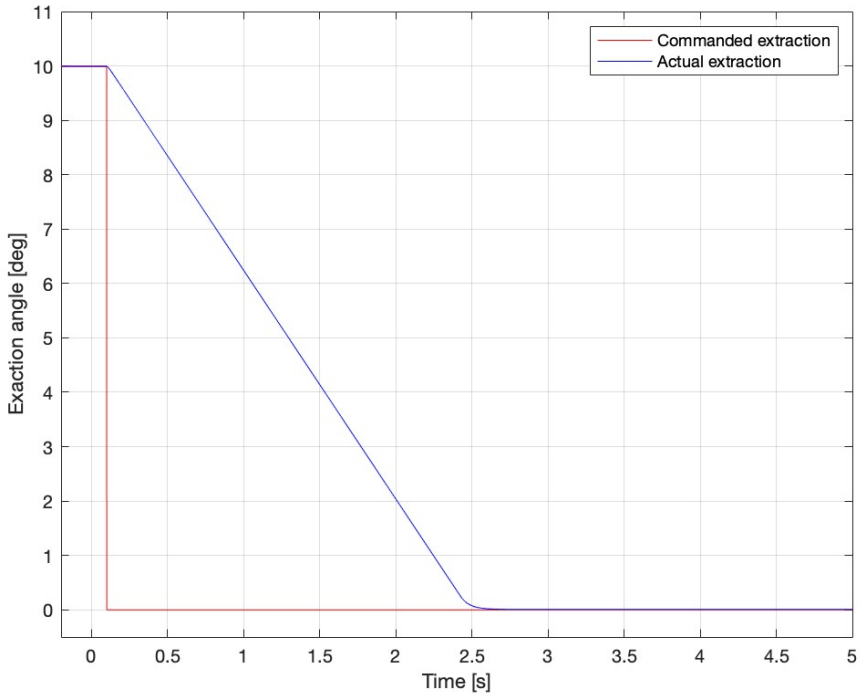

Figure 52: Flap retraction from 10 degrees

5.4.2 Failure with the control logic implemented

In this section a retraction from a 10 degrees position with a failure is now considered. As the previous cases the failure is injected in the system at about the half retraction time, that is around 1.5 seconds after the command is given. Both of the surfaces had reached the position of approximately 4 degrees at the time of the failure. Immediately after the failure the left surface is left without moving torque, so the No-Back Brake implemented in the left half-wing starts working in order to stop the surface from moving freely under the aerodynamic loads. Immediately after the left surface stopped its motion the control logic notes that and starts a compensating action in order to mitigate the actuation asymmetry, once the maximum possible difference between the two extraction positions the control logic commands also the stop of the right surface movement. Around 0.2 seconds after the failure the actuation is completely stopped. In collaboration with the control logic, that mitigates the consequences of the power transmission line failure, the ailerons motion is commanded by the autopilot with the purpose of compensating the roll angle that is caused by the flap asymmetry.

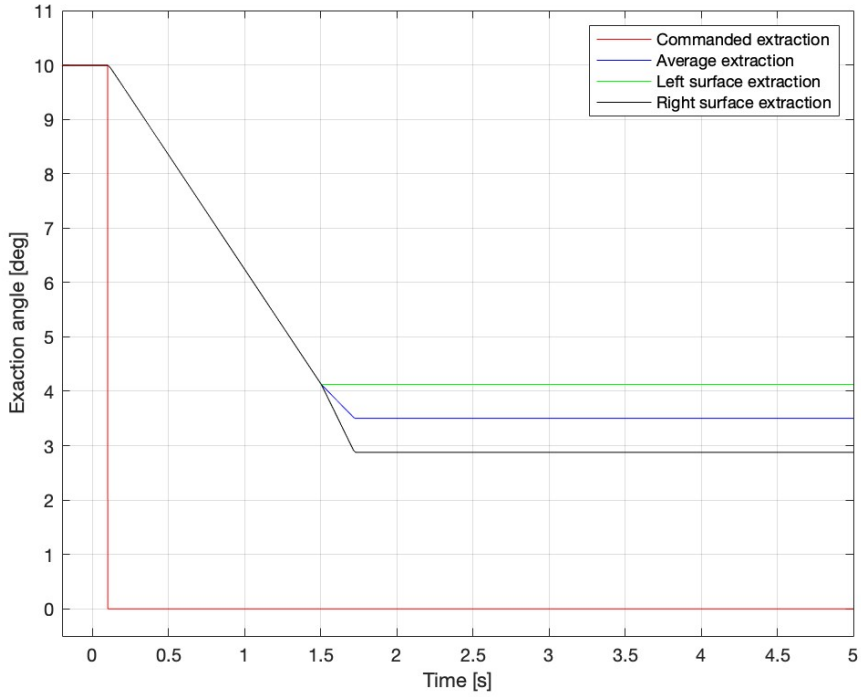

Figure 53: Flap retraction from 10 degrees with failure and controller

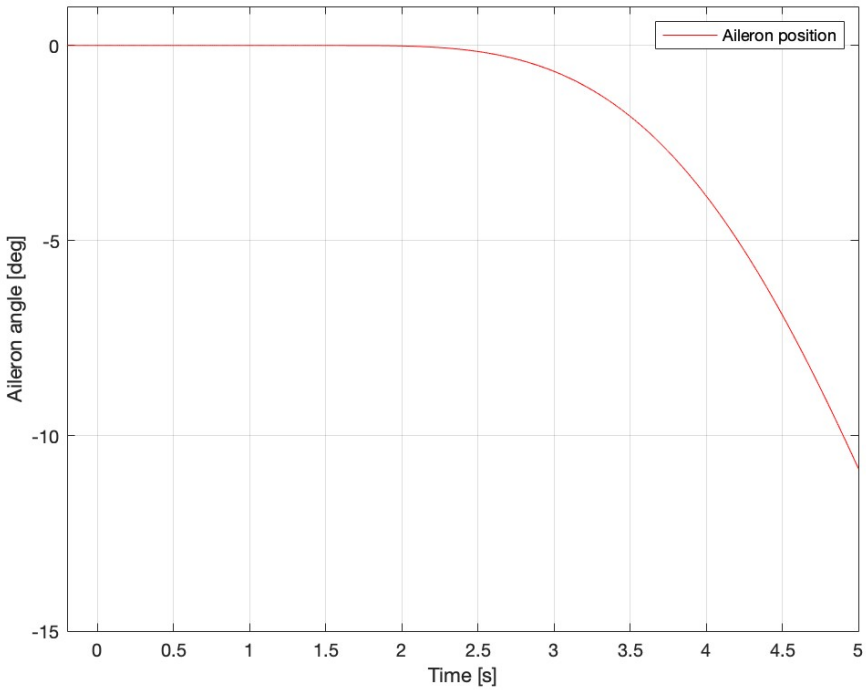

Figure 54: Aileron behavior

5.4.3 Failure without the control logic implemented

The simulation is conducted in the same way of the latter. In the model used for this particular case the control logic was turned off, so no flat asymmetry control and mitigation is performed by the flap actuation system. After the failure that occurs, again, at 1.5 seconds from the beginning of the actuation the left surface movement is blocked by its No-Back Brake. Given the fact that the control logic is not working at this time the right surface continues to be retracted until the neutral position is reached. The asymmetry that is now created is of about 4 degrees, which is four times higher than the operational limit selected for this thesis. It is possible to note that the ailerons are fully extracted in a very short period of time and they have reached the maximum limit of 25 degrees without having compensated the flap asymmetry.

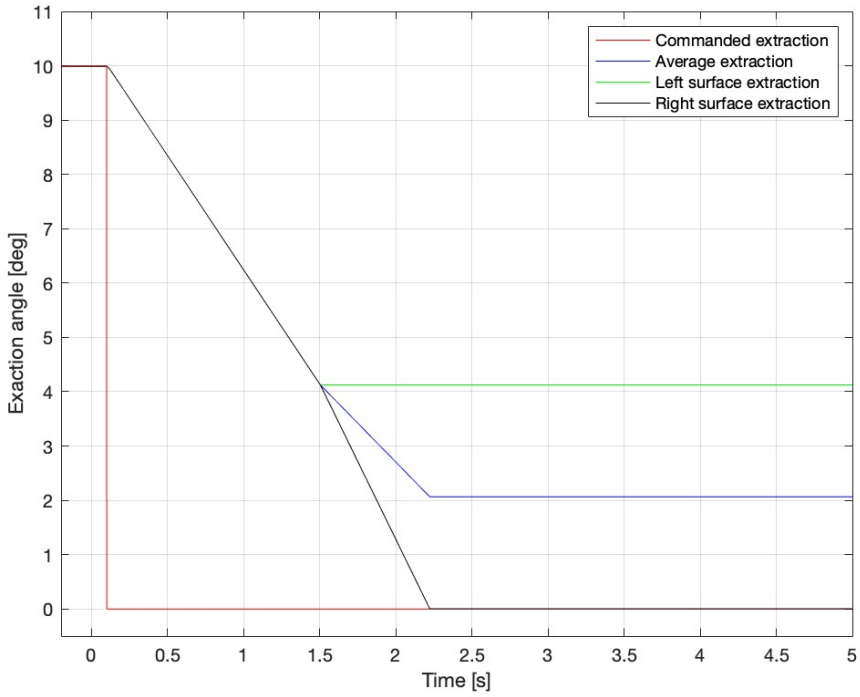

Figure 55: Flap retraction from 10 degrees with failure and no controller

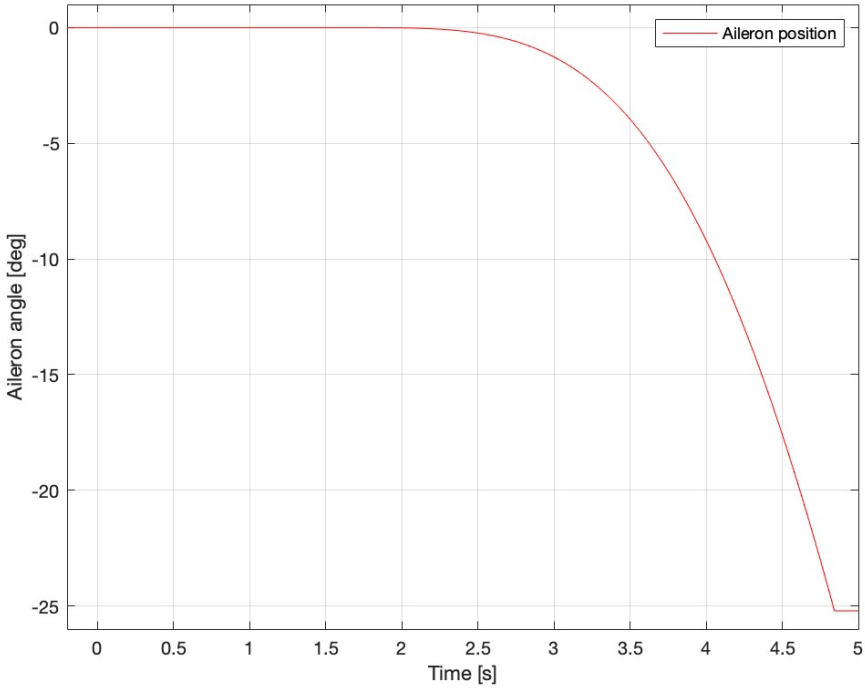

Figure 56: Aileron behavior

5.5 Flap retraction from a 30 degrees position

This simulation case is conducted with an extraction to a position of 30 degrees and then the relative retraction. As stated before, in the following plots the extraction phase is excluded since it is not the focal point of this simualtion case.

5.5.1 Nominal case

This plot shows the nominal simulation case. Initially, the surfaces are positioned at a 30-degree extraction angle. Subsequently, a 30-degree retraction command is received by the flap actuation system. The retraction occurs in a small amount of time, taking approximately 7 seconds.

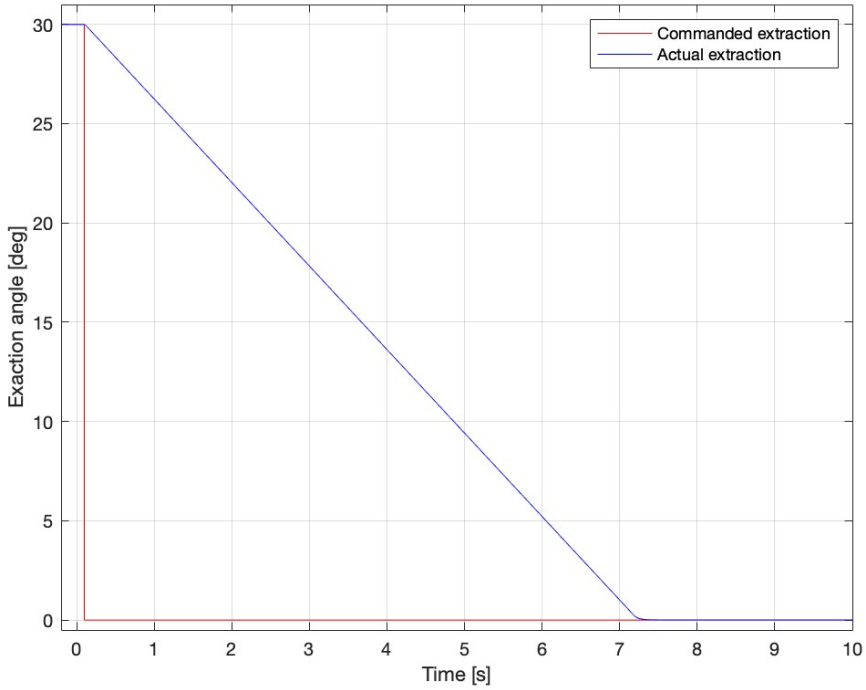

Figure 57: Flap retraction from 30 degrees

5.5.2 Failure with the control logic implemented

This section examines a retraction from a 30-degree position with an introduced failure. Dissimilar to previous cases, the failure is injected into the system almost at the beginning of the retraction, approximately 1.5 seconds after the command is issued. At the moment of failure, both surfaces had reached about 24 degree posiextraction. Immediately following the failure, the left surface loses its driving torque, triggering the No-Back Brake on the left half-wing to engage and prevent the surface from moving freely due to aerodynamic forces. Once the left surface stops moving, the control logic detects this and initiates a compensatory action to reduce the actuation asymmetry. When the maximum allowable difference between the two surfaces' positions is reached, the control logic commands the right surface to halt as well. Approximately 0.2 seconds after the failure, actuation is fully stopped. In coordination with the control logic—which helps mitigate the effects of the power transmission failure—the autopilot commands the ailerons to move, compensating for the roll angle caused by the flap asymmetry.

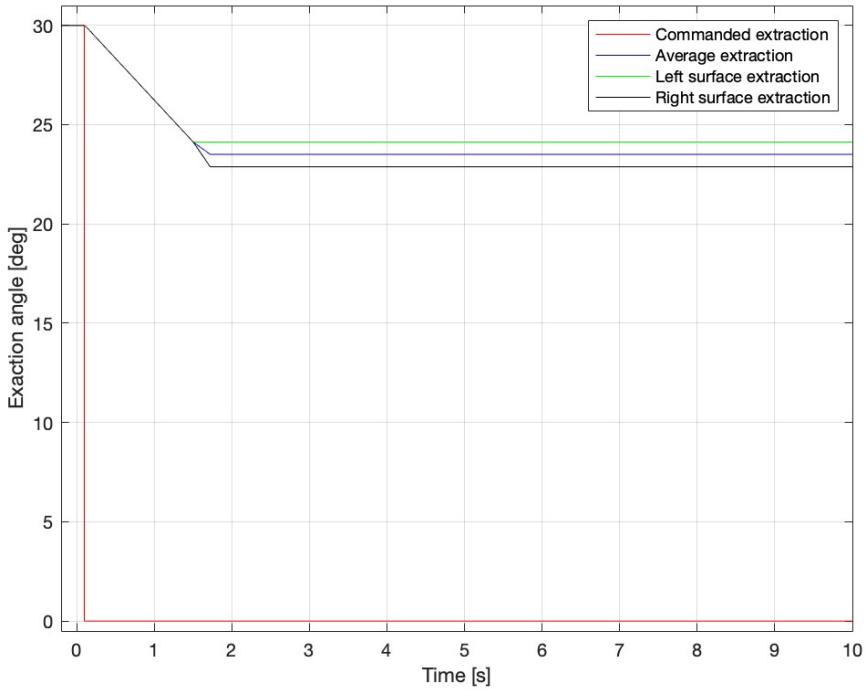

Figure 58: Flap retraction from 10 degrees with failure and controller

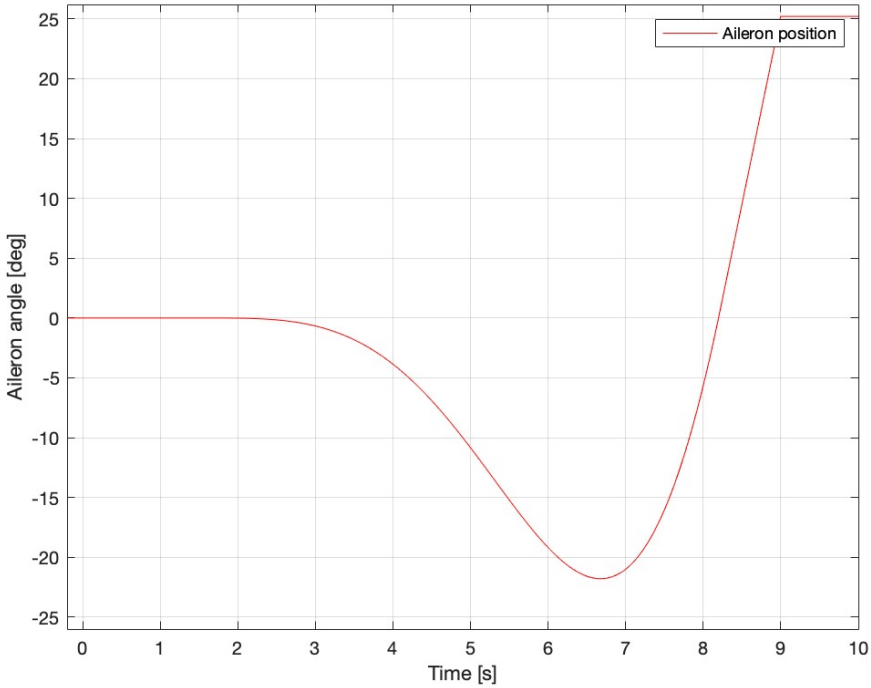

Figure 59: Aileron behavior

5.5.3 Failure without the control logic implemented

The simulation is carried out in the same manner as the previous one. However, in this particular model, the control logic is disabled, so no flap asymmetry control or mitigation is performed by the flap actuation system. After the failure occurs again at 1.5 seconds into the actuation the left surface is halted by its No-Back Brake. Since the control logic is inactive, the right surface continues retracting until it reaches the neutral position. This creates an asymmetry of about 24 degrees, which is many times greater than the operational limit defined for this study. It is also evident that the ailerons fully extend very quickly, reaching their maximum limit of 25 degrees without compensating for the flap asymmetry. This is a difficult scenario for the plane to handle since an asymmetry of 24 degrees creates a high roll moment that is impossible to compensate with the ailerons action.

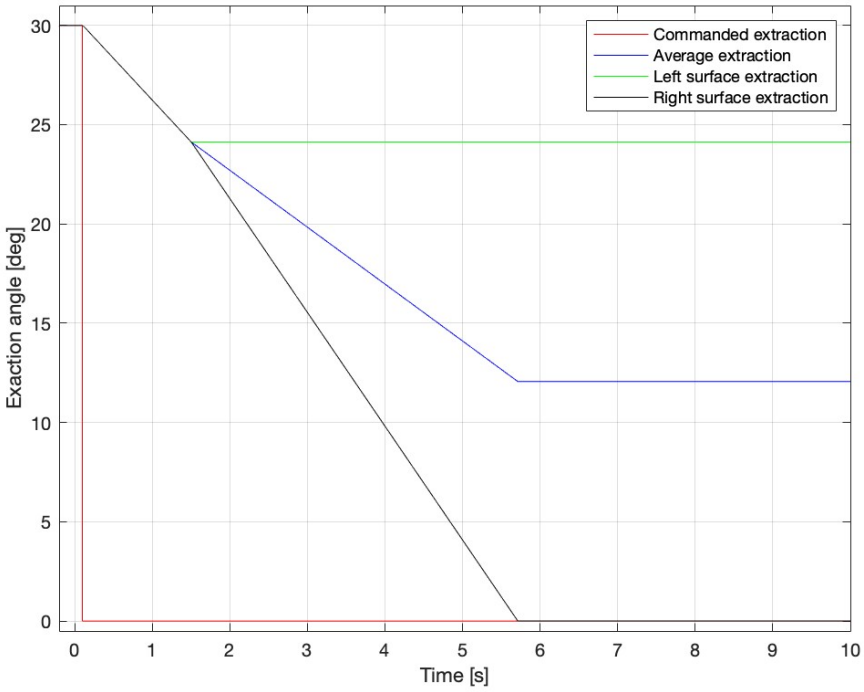

Figure 60: Flap retraction to 30 degrees with failure and no controller

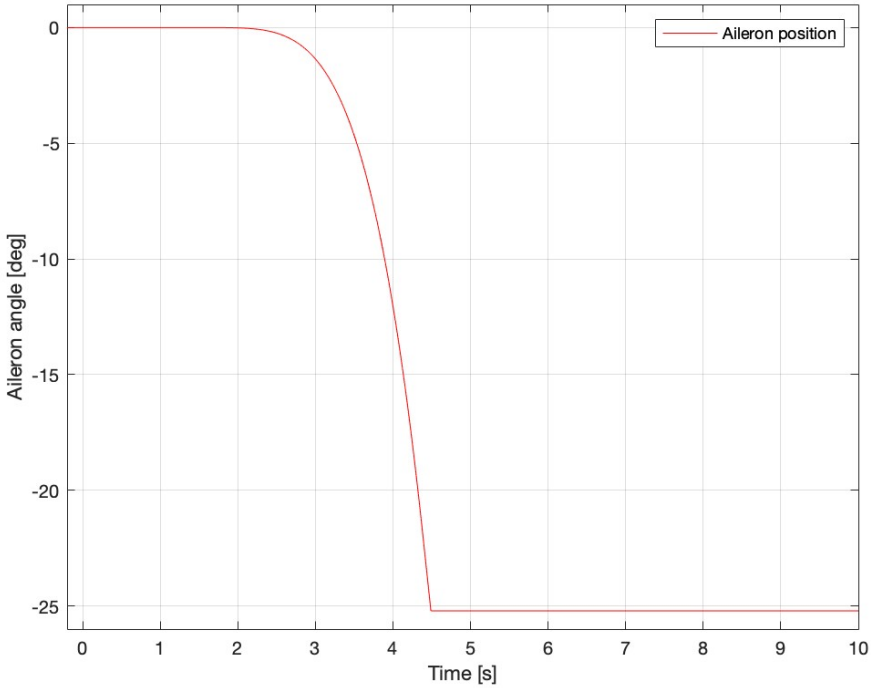

Figure 61: Aileron behavior

5.6 Simulation data and configuration

```
%% Data Flap_Actuation_System

clear
clc
DT                    = 2e-5;            % [s]
   Integration dt

%% controller

controller.GAPm1      = 1e5;             % [1/s]
   controller proportional gain
controller.GAPm2      = 0.05;            % [Nms/rad]
              PID proportional gain
controller.W_refMax   = 8000*pi/30;      % [rad/s]
   position error saturation
controller.I_Max      = 100;             % [A]
   I_ref saturation

%% electrical model

electrical.Z          = 0.5;             % []
   Eccentricity Z
electrical.phi        = 1;               % [rad]
   Eccentricity phi
electrical.P          = 8;               % []
   # poles
electrical.Nabc       = [1 1 1];         % []
   Active coils
electrical.Vdcm       = 48;              % [V]
   Supply voltage
electrical.Rm         = 2.130;           % [ohm]
   Motor R
electrical.Lm         = 720*1e-6;        % [H]
   Motor L
electrical.Kv         = 0.0634;          % [Nm/A]
   K motor
electrical.Ke         = 0.0634;          % [Nm/A]
   K back-emf
electrical.GT         = 0.1634;          % [Nm/A]
   Torque gain
electrical.TMM        = 14.81;           % [Nm]
   Torque saturation

%% mechanical model

mechanical.Jm         = 2.5e-5;          % [kg m^2]
   Inertia
mechanical.Cm         = 5.172e-5;        % [Ns/m]
   Viscous friction
mechanical.BLK        = 1e-5;            % [m]
   Backlash width
mechanical.FST        = 0.1;             % [%]
   Static friction
mechanical.FDT        = 0.05;            % [%]
   Dynamic friction

%% intermetiate shaft
```

```
mechanical.ZM        = 0.0850;          % []
   Z fast-int shaft
mechanical.ZS        = 0.002;           % []
   Z int-slow shaft
mechanical.ZT=mechanical.ZM*mechanical.ZS;
   % Z total
mechanical.BLG       = 0.00056;         % [m]
   Displacement

%% areo loads
load.TRC             = 5000;            % [Nm]
   Aerodynamic load torque
load.TRC0            = 0;               % [Nm]
   I.C. Aerodynamic load torque
load.TRCt            = 0;               % [s]
   Torque application instant


%% surface + actuator
S.CS                 = 8000;            % [N*s/m]
   Dumping coeff
S.JS                 = 407.4;           % [N*s/m]
   Viscous coeff
S.ThSMax             = 40/180*pi;       % [rad]
   Flap maximum extraction
S.ThSMin             = 0;               % [rad]
   Flap retracted position
S.ThS0               = 0*pi/180;        % [rad]
   I.C. surface position
S.ThM0=S.ThS0/mechanical.ZM/mechanical.ZS;
   % Initial motor angular position

%% friction parameters
F.FDS                = 1000;            % [Nm]
   Static friction torque
F.FSS                = 2000;            % [Nm]
   Dynamic friction torque

%%  control logic
DeltaMax             = 0.02;            % [rad]
   Max flap asymmetry
DeltaMaxM            = 0.03;            % [rad]
   Max flap asymmetry to force stop
DDeltaMax            = 0.1;             % [rad/s]
   Max velocity asymmetry
DDeltaMRL            = 0.01;            % [rad]
   Max difference |ThM-ThR|-|ThM-ThL|

%% roll model - autopilot - ailerons model

roll.SNA             = 140;             % [rad]
   Ailerons phi
roll.ZeA             = 0.6;             % []
   Ailerons Z
roll.DThAM           = 0.55;            % [rad/s]
   Max DTh aileron
roll.ThAM            = 0.44;            % [rad]
   Max Th aileron
autopilot.GAP        = -0.8;            % []
   PID proportional gain
```

```
autopilot.GAI        = -0.7;              % [1/s]
   PID integrative gain
autopilot.GAD        = -0.5;              % [s]
   PID derivative gain
RhoA                 = 1.225;             % [kg/m^3]
   Air density
TAS                  = 100;               % [m/s]
   TAS
JXX                  = 161034.56679;      % [kg m^2]
   Jxx inertia
roll.SNDR            = 1.0654;            % [rad]
   Dutch roll phi
roll.ZeDR            = 0.0093;            % []
   Dutch roll Z
```

6 Conclusions

In this thesis it was proven that the extraction of the high-lift surfaces for a business jet aircraft, such as the Lockheed Jetstar is possible. The flap actuation system model can be modified and improved with future developments, such as:

- **Distributed architecture implementation**: A distributed architecture can lead to a even lighter flap actuation system. This is possible by replacing the two big and powerful electrical motors with smaller ones located in the wing structure; by doing so almost every power-transmission shaft can be taken away from the airplane: this makes the flap actuation system lighter and more reliable because there will be less failure critical points. By distributing the actuation into more than one section for each half-wing is also possible to continue use part of the high-lift surfaces on an half-wing in case an anomaly is present.
- **Electrical motor re-design**: the electrical motor chosen for this case-study was a COTS component, but in a real application of this flap actuation system architecture a manufacturer can request to a company specialized in Electrical motors for aeronautical applications to design a specific set of motors and controllers in order to enhance the performances of the system.
- **Control logic improvement**: the control logic implemented in this simulation is very simple and accounts only on the differences between the angular positions and the angular velocities of the two surfaces. The improvements can be done with different modifications, by limiting even more the angular displacement allowed, by implementing a logic that is self-adapting to each specific use case or by lowering the time needed to have a full stop of the second surface after the failure is detected.

A possible future implementation of this model can be done with a larger plane, where the aerodynamic loads are much higher. With the continuous development the technologies future electrical motors will be capable of the generation of even greater mechanical torques that can actuate the high-lift system of a commercial liner.

7 Bibliography

- **Mechanical failures of flap control systems: proposal of advanced monitoring techniques**, L. Borello and G. Villero, Journal of Mechanics and Control, 2004
- **Aircraft Flap Control System: Proposal of a Simulink Test Bench for Evaluating Innovative Asymmetry Monitoring and Control Techniques**, D. Belmonte, M.D.L. Dalla Vedova and P.Maggiore, Politecnico di Torino, 2016
- **Design and development of algorithms and technologies applied to prognostics of aerospace systems**, P. Berri, Politecnico di Torino, 2021
- **Modellazione, simulazione e sperimentazione dei sistemi aerospaziali**, course slides, M.D.L. Della Vedova, Politecnico di Torino, "2024
- **Meccanica del Volo**, course slides, P. Gili, Politecnico di Torino, 2023
- **Guida e Controllo del Velivolo**, course slides, M. Battipede, Politecnico di Torino, 2023